

Recent Developments on and Prospects for Electrode Materials with Hierarchical Structures for Lithium-Ion Batteries

Limin Zhou, Kai Zhang, Zhe Hu, Zhanliang Tao,* Liqiang Mai, Yong-Mook Kang, Shu-Lei Chou,* and Jun Chen

Since their successful commercialization in 1990s, lithium-ion batteries (LIBs) have been widely applied in portable digital products. The energy density and power density of LIBs are inadequate, however, to satisfy the continuous growth in demand. Considering the cost distribution in battery system, it is essential to explore cathode/anode materials with excellent rate capability and long cycle life. Nanometer-sized electrode materials could quickly take up and store numerous Li^+ ions, afforded by short diffusion channels and large surface area. Unfortunately, low thermodynamic stability of nanoparticles results in electrochemical agglomeration and raises the risk of side reactions on electrolyte. Thus, micro/nano and hetero/hierarchical structures, characterized by ordered assembly of different sizes, phases, and/or pores, have been developed, which enable us to effectively improve the utilization, reaction kinetics, and structural stability of electrode materials. This review summarizes the recent efforts on electrode materials with hierarchical structures, and discusses the effects of hierarchical structures on electrochemical performance in detail. Multidimensional self-assembled structures can achieve integration of the advantages of materials with different sizes. Core/yolk-shell structures provide synergistic effects between the shell and the core/yolk. Porous structures with macro-, meso-, and micropores can accommodate volume expansion and facilitate electrolyte infiltration.

1. Introduction


Since their commercialization by Sony Corporation in the early 1990s, lithium-ion batteries (LIBs) have been widely utilized as energy supplies for portable devices such as laptop computers,

mobile phones, and digital cameras.^[1–6] Recently, LIBs have also been intensively pursued as an energy-storage technology for electrical vehicles and stationary power stations.^[7–10] The reaction equations, structures, and costs of the individual components of LIBs with the common LiCoO_2 ||polymer electrolyte||graphite system are shown in Figure 1. It can be seen that cathode and anode materials, which serve as the most important components of LIBs, largely decide the electrochemical performance and cost of the batteries. According to the intrinsic features and reaction mechanisms of materials, four types of cathode materials and three sorts of anode materials have been investigated.^[11–16] The traditional electrode material LiCoO_2 is hindered, however, by its relatively low specific capacity and the high price of Co resources, along with its inferiority in terms of environmental friendliness. LiMn_2O_4 suffers from the Jahn–Teller distortion of Mn^{3+} and the dissolution of Mn^{2+} in the electrolyte, resulting in severe capacity attenuation

and poor cycling performance. Graphite, as the most widely employed anode material, is limited by its finite capacity. Though $\text{Li}_4\text{Ti}_5\text{O}_{12}$ typically offers excellent cycle life and high safety, its relatively high potential would entail low energy density. In contrast, high-capacity Si material cannot offer long

Dr. L. M. Zhou, Prof. Z. L. Tao, Dr. S.-L. Chou, Prof. J. Chen
Key Laboratory of Advanced Energy Materials Chemistry
(Ministry of Education)
Collaborative Innovation Center of Chemical Science and Engineering
College of Chemistry
Nankai University
Tianjin 300071, P. R. China
E-mail: taozhl@nankai.edu.cn

Dr. L. M. Zhou, Prof. L. Q. Mai
State Key Laboratory of Advanced Technology for
Materials Synthesis and Processing
Wuhan University of Technology
Hubei, Wuhan 430070, P. R. China

 The ORCID identification number(s) for the author(s) of this article can be found under <https://doi.org/10.1002/aenm.201701415>.

Dr. K. Zhang, Prof. Y.-M. Kang
Department of Energy and Materials Engineering
Dongguk University, Seoul
100-715, Republic of Korea

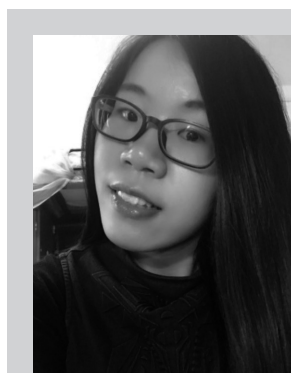
Dr. Z. Hu, Dr. S.-L. Chou
Institute for Superconducting and Electronic Materials
University of Wollongong
Wollongong, New South Wales 2522, Australia
E-mail: shulei@uow.edu.au

DOI: 10.1002/aenm.201701415

cycle life. Therefore, many cathode and anode materials have been investigated to make up for the deficiency of these traditional electrode materials.

Table 1 summarizes representative cathode and anode materials with their basic electrochemical properties. Concretely, cathode materials principally consist of high-capacity layered transition-metal oxides, such as LiCoO_2 , $\text{LiCo}_{1/3}\text{Ni}_{1/3}\text{Mn}_{1/3}\text{O}_2$, and $\text{LiMn}_{0.8}\text{Co}_{0.15}\text{Al}_{0.05}\text{O}_2$; high-potential Mn-based spinels, such as $\text{LiNi}_{0.5}\text{Mn}_{1.5}\text{O}_4$; and highly stable polyanion-type compounds, such as LiFePO_4 . The anode materials are mainly insertion-reaction-type materials, such as graphite and $\text{Li}_4\text{Ti}_5\text{O}_{12}$; alloying reaction-type elements, such as Sn, Ge, and Si; and conversion reaction-type oxides/sulfides, such as Fe_2O_3 and MoS_2 . Actually, each has its own merits and deficiencies. High-capacity layered transition-metal oxides suffer from O_2 evolution at high charging potentials, leading to serious safety issues for practical application.^[15] High-potential Mn-based spinels feature low cost and environmental friendliness, but Mn dissolution and Jahn–Teller distortion destroy the spinel structure, resulting in capacity decay during cycling.^[3] Polyanion-type compounds feature high thermal stability, environmental compatibility, and low price. Nevertheless, they face the challenge of low conductivity, which has a negative impact on their rate performance.^[17] For anode, high-capacity materials such as Si, Sn, and Fe_2O_3 are always accompanied by huge volume expansion; while the materials with small volume changes, such as graphite and $\text{Li}_4\text{Ti}_5\text{O}_{12}$, mostly have low theoretical specific capacity.^[18]

To overcome the above deficiencies of these materials, nanoparticles are able to shorten diffusion distances, enhance electronic conductivity, and alleviate the mechanical stress generated during charge/discharge process, further contributing to the rate capacity and cycling stability. Their low thermodynamic stability, however, does not allow nanoscale materials to be accepted and practically applied, because their instability would inevitably give rise to agglomeration during electrode production and repeated cycling, resulting in quick capacity fading. In addition, the high rate of surface reactions between the electrode and electrolyte also leads to a poor cycle life and a large degree of irreversibility.^[19] Therefore, another superior approach, hierarchical structure design, has been attempted. Hierarchical structures integrate the merits of materials with different sizes (microsize/nanosize), phases (layered compounds/spinel/perovskite/olivine), and pores (macropore/mesopore/micropore), which makes them assemble in an orderly way into various favorable morphologies.^[3,20,21] So far, three hierarchical structures have been designed and used to improve the electrochemical performance of cathode and anode materials, namely, multidimensional self-assembled structures, core/yolk–shell structures, and porous structures (**Figure 2**). Multidimensional self-assembled structures combine the fast kinetics of nanomaterials with the high tap density of micromaterials, which mainly include two types of architecture: microstructures assembled from nanostructures (e.g., nanoparticle-assembled $\text{LiNi}_{1/3}\text{Co}_{1/3}\text{Mn}_{1/3}\text{O}_2$ microspheres)^[22] and nanoparticles embedded in a micro-matrix (e.g., ultrasmall Sn nanoparticles embedded in carbon spheres).^[23] Core/yolk–shell structures consist of at least two materials which afford their respective advantages. For instance, $\text{Li}(\text{Ni}_{0.8}\text{Co}_{0.1}\text{Mn}_{0.1})_{0.8}$



Limin Zhou received her M.S. degree from College of Chemistry at Nankai University in 2015. She is currently working toward the Ph.D. degree in Materials Engineering from Wuhan University of Technology. Her current research focuses on synthesis and characterization of advanced materials for sodium-ion batteries.



Kai Zhang received his Ph.D. in 2015 and B.S. in 2010 from College of Chemistry at Nankai University (China) under the supervision of Professor Jun Chen. Currently, he is a postdoctoral researcher in the group of Professor Yong-Mook Kang at the Department of Energy and Materials Engineering in Dongguk University, Seoul, Korea. His research focuses on lithium-ion, lithium-sulfur, and sodium-ion batteries.



Zhanliang Tao received his Ph.D. in Inorganic Chemistry from Nankai University in 2005. He has been an associated professor at the Key Laboratory of Advanced Energy Materials Chemistry (Ministry of Education) since 2008. His current research interests are focused on light weight nanomaterials for energy storage and conversion.

$(\text{Ni}_{0.5}\text{Mn}_{0.5})_{0.2}\text{O}_2$ has a highly stable shell (i.e., $\text{LiNi}_{0.5}\text{Mn}_{0.5}\text{O}_2$) and a high-capacity core (i.e., $\text{LiNi}_{0.8}\text{Co}_{0.1}\text{Mn}_{0.1}\text{O}_2$).^[24] Porous structures are materials containing multidimensional pores (i.e., macro, meso, and micropores), and they achieve the aim of “something from nothing.” Namely, the improved electrochemical performance originates from porosity. The superiority of porous structure reflects in three aspects: micropores can store Li^+ ions, mesopores provide Li^+ transport channels, and macropores accommodate the volume expansion.^[25]

Various materials with hierarchical structures have recently been used to develop electrodes for LIBs. The results of theoretical calculations and experiments prove that the interactions and synergistic effects of different sizes, pores, morphologies, and phases contribute to the electrochemical reactions during

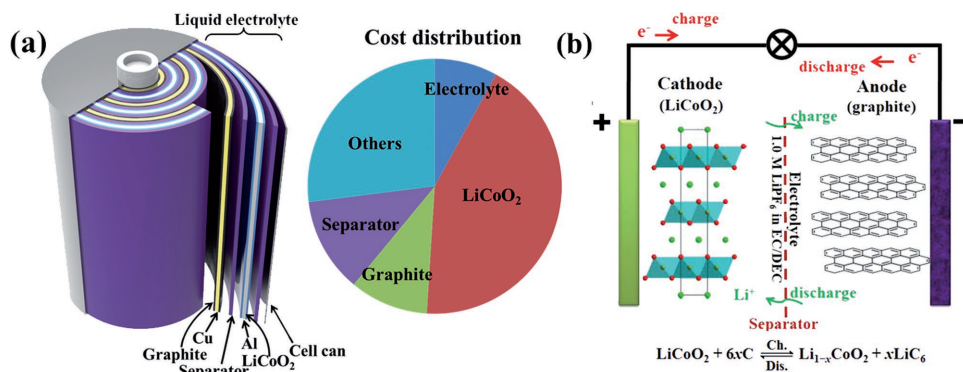


Figure 1. a) Structural illustration and relative cost of each component of commercial cell. b) The reaction equation and charge/discharge process for LIBs with LiCoO₂ cathode and graphite anode.

the charge/discharge process. In this review, recent studies on hierarchically structured materials for LIBs are summarized. The preparation of hierarchical structures is briefly introduced, and the effects of the hierarchical structures on the electrochemical performance of the electrode materials are discussed in detail. In addition, the challenges and prospects for electrode materials with hierarchical structures are also proposed.

2. Cathode Materials

Cathode materials play a key role in the capacity, output voltage, and cost of LIBs. Among them, LIBs with LiCoO₂ as the cathode material have widely occupied the field of consumer electronic devices. The practical specific capacity of LiCoO₂ only reaches 140 mAh g⁻¹, however, and Co resources have a high price.^[26] To meet the demand for high energy density, low cost, and reliable safety, various compounds with hierarchical

structures have been reported, such as high-capacity layered transition-metal oxides, high-potential Mn-based spinels, and highly stable polyanion-type compounds.

2.1. Layered Transition-Metal Oxides

In the layered transition-metal oxides, Li and M (M = metal) cations occupy the octahedral voids of O-arrays. The Li layer lies between two neighboring MO₆ octahedral layers, and Li ions have 2D diffusion paths.^[15] LiMO₂ (M = Co and Ni) is the most famous class of layered transition-metal oxides, which have a hexagonal α-NaFeO₂ structure with Rm space group (Figure 3a).^[27] For LiCoO₂, the t_{2g} band of redox active Co⁴⁺/Co³⁺ significantly overlaps with the top of the 2p band of O²⁻ ions (Figure 3b), leading to a loss of O₂ when x exceeds 0.5 in Li_{1-x}CoO₂. Thus, it is difficult for the discharge capacity

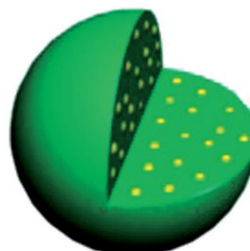
Table 1. Reaction mechanisms, theoretical specific capacities [Q/mAh g⁻¹], redox potentials [E/V], and remarks on some representative electrode materials for LIBs.

Type	Material	Reaction mechanism	Q	E	Remarks	
Cathode Layered transition-metal oxides	LiCoO ₂	LiCoO ₂ ↔ CoO ₂ + Li ⁺ + e ⁻	274	3.9	High cost, O ₂ release at more than 4.3 V	
	LiNi _{1/3} Co _{1/3} Mn _{1/3} O ₂	LiNi _{1/3} Co _{1/3} Mn _{1/3} O ₂ ↔ Ni _{1/3} Co _{1/3} Mn _{1/3} O ₂ + Li ⁺ + e ⁻	278	3.8	Stable structure, inferior rate capability	
	LiNi _{0.8} Co _{0.15} Al _{0.05} O ₂	LiNi _{0.8} Co _{0.15} Al _{0.05} O ₂ ↔ Ni _{0.8} Co _{0.15} Al _{0.05} O ₂ + Li ⁺ + e ⁻	279	3.8	High practical capacity, cation disordering of Li and Ni ions	
Mn-based spinels	LiMn ₂ O ₄	LiMn ₂ O ₄ ↔ 2λ-MnO ₂ + Li ⁺ + e ⁻	148	4.0	Jahn–Teller distortion, Mn dissolution	
	LiNi _{0.5} Mn _{1.5} O ₄	LiNi _{0.5} Mn _{1.5} O ₄ ↔ Ni _{0.5} Mn _{1.5} O ₄ + Li ⁺ + e ⁻	147	4.7	Electrolyte/structural instability under high potentials	
Polyanion-type compounds	LiFePO ₄	LiFePO ₄ ↔ FePO ₄ + Li ⁺ + e ⁻	170	3.45	Excellent cycling stability, low conductivity	
	Li ₂ MnSiO ₄	Li ₂ MnSiO ₄ ↔ MnSiO ₄ + 2Li ⁺ + 2e ⁻	331	4.1	Poor cycling performance, low conductivity	
Anode	Insertion type	Graphite	6C + Li ⁺ + e ⁻ ↔ LiC ₆	372	0.1	Low capacity
		Li ₄ Ti ₅ O ₁₂	Li ₄ Ti ₅ O ₁₂ + 3Li ⁺ + 3e ⁻ ↔ Li ₇ Ti ₅ O ₁₂	175	1.55	High safety, low capacity
	Alloying type	Si	5Si + 22Li ⁺ + e ⁻ ↔ Li ₂₂ Si ₅	4197	0.1	Low conductivity, large volume expansion
		Sn	5Sn + 22Li ⁺ + e ⁻ ↔ Li ₂₂ Sn ₅	993	0.5	Large volume expansion
		P	P + 3Li ⁺ + 3e ⁻ ↔ Li ₃ P	2594	1.0	Low conductivity, large volume expansion
Conversion type	Fe ₂ O ₃	Fe ₂ O ₃ + 6Li ⁺ + e ⁻ ↔ 2Fe + 3Li ₂ O	1007	0.9	Large structural change and volume expansion	

(a) Multi-dimensional self-assembled structure

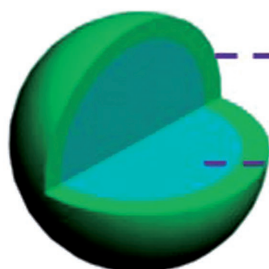


**Nanoparticle-assembled
microarchitecture**



**Nanoparticles embedded
in a micro-matrix**

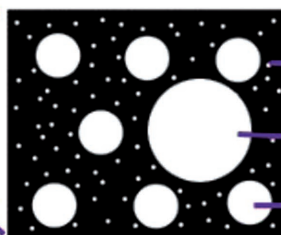
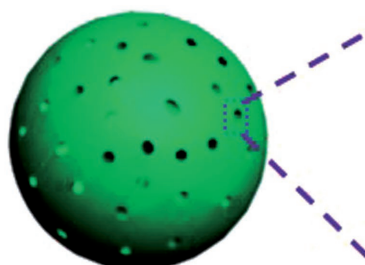
(b) Core-shell/yolk-shell structure



**Highly stable or
conductive shell**

**High-capacity or
high voltage core**

(c) Porous structure



micropore

macropore

mesopore

Figure 2. Schematic illustration of three hierarchical structures: a) multidimensional self-assembled structure, b) core-shell/yolk-shell structure, c) porous structure.

of LiCoO_2 to reach more than 140 mAh g^{-1} . In order to improve the practical capacity and structural stability, high-capacity Ni-rich layered transition-metal oxides and highly stable Ni/Mn-based layered transition-metal oxides are proposed.

2.1.1. Ni-Rich Layered Transition-Metal Oxides

Ni-rich layered transition-metal oxides originate from high-capacity LiNiO_2 . Since the e_g band of redox active $\text{Ni}^{4+}/\text{Ni}^{3+}$ only slightly overlaps the top of the $2p$ band of O^{2-} ions in $\text{Li}_{1-x}\text{NiO}_2$ (Figure 3c), LiNiO_2 can obtain a capacity of $\approx 200 \text{ mAh g}^{-1}$ when cycling in the range of $0 \leq x \leq 0.75$. LiNiO_2 is plagued by nonstoichiometric structures, structural degradation, and capacity fading, however, due to the migration of Ni^{3+} ions

to the Li layer. In order to improve the thermal stability and improve the performance degradation, cation-substituted layered transition-metal oxides as well as structural doping have been investigated. Among the various $\text{LiCo}_{1-x}\text{Ni}_x\text{O}_2$ ($x = 0-1$) compounds, $\text{LiNi}_{0.8}\text{Co}_{0.2}\text{O}_2$ showed the best electrochemical performance.^[28] Due to the phase transitions and lattice changes, as well as the side reactions between electrode and electrolyte during the charge/discharge process, partial substitution of an electrochemically inert metal for Ni or Co and surface coating with inactive materials are adopted to enhance the electrochemical performance. ZrO_2 nanoparticles were deposited on the surface of $\text{LiNi}_{0.8}\text{Co}_{0.2}\text{O}_2$ to suppress impedance growth during cycling.^[29] With further substitution by Mn or Al, $\text{LiNi}_{0.8}\text{Co}_{0.1}\text{Mn}_{0.1}\text{O}_2$ and $\text{LiNi}_{0.8}\text{Co}_{0.15}\text{Al}_{0.05}\text{O}_2$ can achieve better cycling and rate performance.

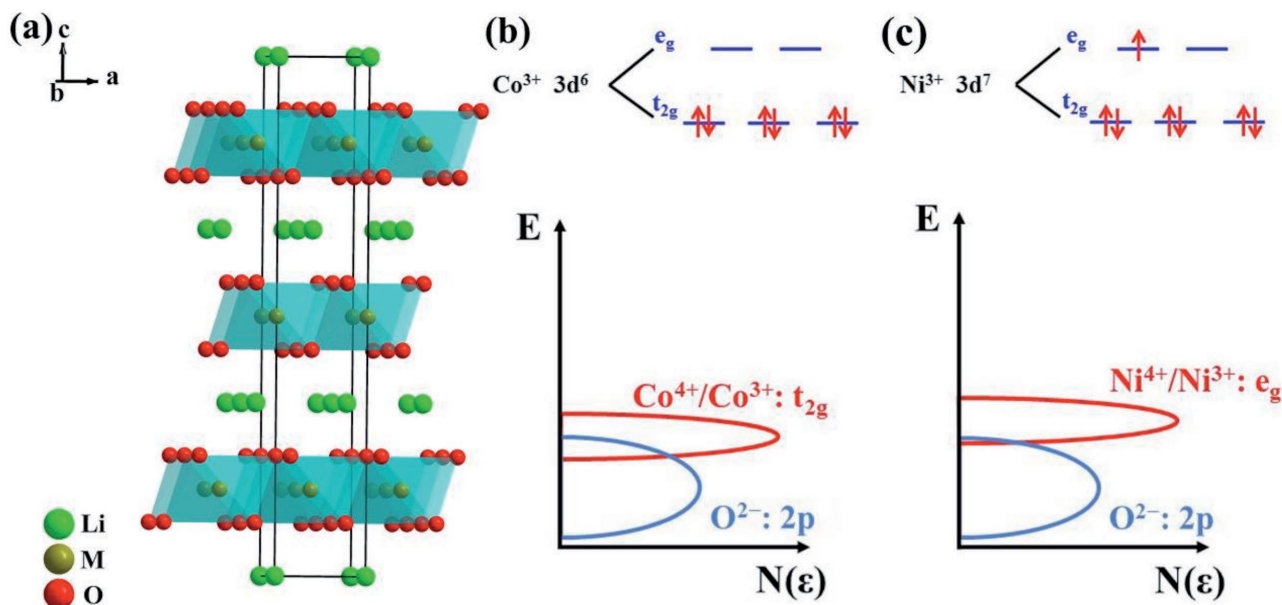


Figure 3. a) Crystal structure of layered LiMO_2 ($M = \text{Co}$ and Ni). Schematic illustrations of the energy vs. density of states, showing the relative positions of the Fermi energy in an itinerant electron band for b) $\text{Co}^{4+}/\text{Co}^{3+}$ and c) $\text{Ni}^{4+}/\text{Ni}^{3+}$ redox couples for $\text{Li}_{1-x}\text{CoO}_2$ and $\text{Li}_{1-x}\text{NiO}_2$, respectively.

$\text{LiNi}_{0.8}\text{Co}_{0.1}\text{Mn}_{0.1}\text{O}_2$ displays a high capacity of $\approx 200 \text{ mAh g}^{-1}$, but it suffers from a structural transition and the dissolution of Li and Ni ions in the electrolyte during cycling, as well as slight Mn ion dissolution. The assembly of core-shell structures composed of relatively stable materials is an effective approach to realize both high capacity and high surface stability. Li and co-workers prepared Li_2TiO_3 -coated $\text{LiNi}_{0.8}\text{Co}_{0.1}\text{Mn}_{0.1}\text{O}_2$ nanobelts based on the reaction between $\text{Ni}_{0.8}\text{Co}_{0.1}\text{Mn}_{0.1}\text{C}_2\text{O}_4$ and $\text{Ti}(\text{OC}_4\text{H}_9)_4$.^[30] The Li_2TiO_3 layer possessed 3D Li^+ diffusion path, and Ti^{4+} is doped into $\text{LiNi}_{0.8}\text{Co}_{0.1}\text{Mn}_{0.1}\text{O}_2$ with Ni^{2+} and Co^{3+} ions, which is favorable for Li^+ ion transfer at the interface. The Li_2TiO_3 coated $\text{LiNi}_{0.8}\text{Co}_{0.1}\text{Mn}_{0.1}\text{O}_2$ nanobelts displayed a discharge capacity of 130 mAh g^{-1} at 10 C when cycling in the voltage range of 3.0–4.3 V at 55 °C. Some reports have focused on using core-shell structured or concentration-gradient cathodes with highly thermally stable shells or outer layers to improve the cycling stability. $\text{Li}[(\text{Ni}_{0.8}\text{Co}_{0.1}\text{Mn}_{0.1})_{0.8}(\text{Ni}_{0.5}\text{Mn}_{0.5})_{0.2}]\text{O}_2$ with a $\text{LiNi}_{0.8}\text{Co}_{0.1}\text{Mn}_{0.1}\text{O}_2$ core and a $\text{LiNi}_{0.5}\text{Mn}_{0.5}\text{O}_2$ shell was designed and prepared by two-step coprecipitation with a subsequent solid-state reaction.^[24] The core-shell structured cathode delivered capacity retention of 81% after 500 cycles and excellent thermal stability. Nevertheless, in face of the big voids caused by the different stresses endured from the structural mismatch, Sun et al. designed a concentration-gradient cathode composed of a $\text{LiNi}_{0.8}\text{Co}_{0.1}\text{Mn}_{0.1}\text{O}_2$ core, a $\text{LiNi}_{0.8-x}\text{Co}_{0.1+y}\text{Mn}_{0.1+z}\text{O}_2$ ($0 \leq x \leq 0.34$, $0 \leq y \leq 0.13$, and $0 \leq z \leq 0.21$) outer layer, and a $\text{LiNi}_{0.46}\text{Co}_{0.23}\text{Mn}_{0.31}\text{O}_2$ surface to mitigate the structural mismatch problem, and this composite was also synthesized by a two-step coprecipitation with a subsequent solid-state reaction.^[31] Compared with $\text{LiNi}_{0.8}\text{Co}_{0.1}\text{Mn}_{0.1}\text{O}_2$, the concentration-gradient cathode displayed a similar initial discharge capacity but higher capacity retention (96.5% after 500 cycles at 1 C). After slightly diminishing the Ni content, Sun et al. manufactured a full concentration-gradient (FCG) cathode with $\text{LiNi}_{0.86}\text{Co}_{0.1}\text{Mn}_{0.04}\text{O}_2$ as the inner composition (IC) and

$\text{LiNi}_{0.7}\text{Co}_{0.1}\text{Mn}_{0.2}\text{O}_2$ as the outer composition (OC),^[32] which delivered a high capacity of 215 mAh g^{-1} at 0.2 C (Figure 4a,b). Compared with pure IC and OC materials, the FCG materials showed better cycling performance (Figure 4c).

$\text{LiNi}_{0.8}\text{Co}_{0.15}\text{Al}_{0.05}\text{O}_2$ is also a promising cathode material with high capacity, which has been successfully applied in the Tesla automobile. Some Ni^{2+} ions, however, occupy 3a sites of Li^+ ions owing to their similar radii, leading to sluggish kinetics. Some micro/nanostructured spheres have been designed to boost the electrochemical performance.^[33–35] $\text{LiNi}_{0.8}\text{Co}_{0.15}\text{Al}_{0.05}\text{O}_2$ spheres with monodispersed crumpled yolk-shell structures were obtained via a supersonic atomization method with further heat treatment.^[35] The yolk-shell structured $\text{LiNi}_{0.8}\text{Co}_{0.15}\text{Al}_{0.05}\text{O}_2$ showed discharge capacities of 225.9 mAh g^{-1} at 0.1 C and 129.7 mAh g^{-1} at 1 C. Our group employed AlO_2^- as Al sources to synthesize $\text{LiNi}_{0.8}\text{Co}_{0.15}\text{Al}_{0.05}\text{O}_2$ through facile co-precipitation method, which exhibited high rate capability and good cycling stability.^[36] On slightly increasing the Al content, the $\text{LiNi}_{0.81}\text{Co}_{0.1}\text{Al}_{0.09}\text{O}_2$ microspheres assembled from many nanorods exhibited excellent rate capability, with capacity of 155 mAh g^{-1} at 10 C in the voltage range of 3–4.5 V and high thermal stability. Highly stable $\text{LiNi}_{0.5}\text{Mn}_{0.5}\text{O}_2$ was also used to modify the $\text{LiNi}_{0.8}\text{Co}_{0.15}\text{Al}_{0.05}\text{O}_2$.^[37] The core-shell structured $\text{Li}(\text{Ni}_{0.8}\text{Co}_{0.15}\text{Al}_{0.05})_{0.8}(\text{Ni}_{0.5}\text{Mn}_{0.5})_{0.2}\text{O}_2$ was synthesized via a coprecipitation method combined with a solid-state reaction, and it displayed discharge capacities of 195 mAh g^{-1} at 0.1 C and 127 mAh g^{-1} at 5 C. In addition, $\text{LiNi}_{0.915}\text{Co}_{0.075}\text{Al}_{0.01}\text{O}_2$ with a high Ni content (>90%) was also investigated by the coating of SiO_2 and amorphous $\text{Zr}(\text{OH})_4$.^[38,39]

2.1.2. Ni/Mn-Based Transition-Metal Oxides

For the binary Ni/Mn-based transition-metal oxides family $\text{LiNi}_{1-x}\text{Mn}_x\text{O}_2$ ($0 < x < 1$), $\text{LiNi}_{0.5}\text{Mn}_{0.5}\text{O}_2$ shows the best

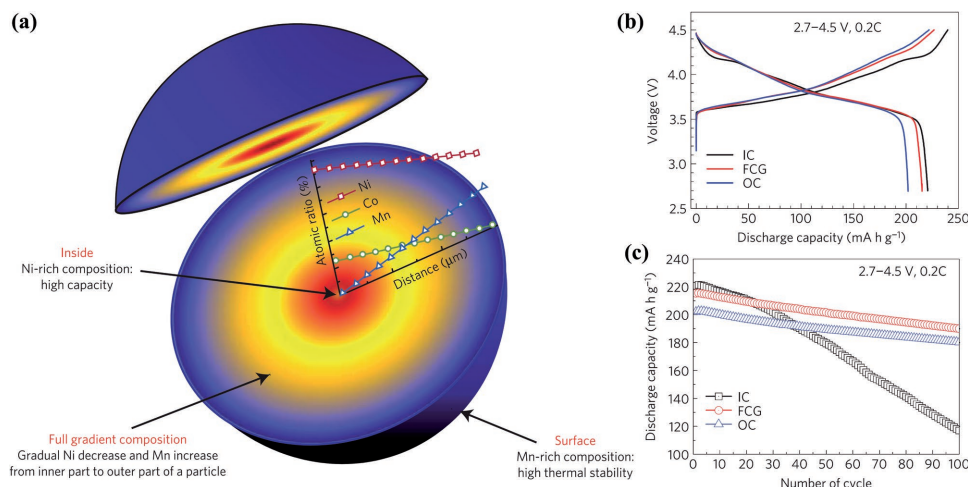


Figure 4. a) Schematic diagram of the FCG cathode with the Ni concentration decreasing from the center toward the outer layer and the Mn concentration increasing accordingly. b) Initial charge–discharge curves and c) cycling performance of FCG, IC, and OC materials. Reproduced with permission.^[32] Copyright 2012, Nature Publishing Group.

structural stability.^[40] To further stabilize the layered structure and enhance the capacity, the $\text{LiCoO}_2\text{-LiNi}_{0.5}\text{Mn}_{0.5}\text{O}_2$ and $\text{Li}_2\text{MnO}_3\text{-LiNi}_{0.5}\text{Mn}_{0.5}\text{O}_2$ systems have been proposed.

$\text{LiCoO}_2\text{-LiNi}_{0.5}\text{Mn}_{0.5}\text{O}_2$ can be represented as $\text{LiNi}_x\text{Mn}_x\text{Co}_{1-2x}\text{O}_2$ ($0 \leq x \leq 0.5$). Li^+ , transition metal (Ni^{2+} , Co^{3+} , Mn^{4+}), and O^{2-} ions are located on 3a, 3b, and 6c sites, respectively. The major electrochemical activity originates from $\text{Ni}^{4+}/\text{Ni}^{3+}/\text{Ni}^{2+}$ couples, and a small additional capacity at high potential is attributed to the $\text{Co}^{4+}/\text{Co}^{3+}$ couple. Among the various $\text{LiNi}_x\text{Mn}_x\text{Co}_{1-2x}\text{O}_2$, $\text{LiNi}_{1/3}\text{Mn}_{1/3}\text{Co}_{1/3}\text{O}_2$ delivered the highest discharge capacity at a high current density.^[41] $\text{LiNi}_{1/3}\text{Mn}_{1/3}\text{Co}_{1/3}\text{O}_2$, which also possesses an O3-type layered structure, was discovered by Ohzuku and Makimura.^[42] $\text{LiNi}_{1/3}\text{Mn}_{1/3}\text{Co}_{1/3}\text{O}_2$ is constructed from a $[\sqrt{3} \times \sqrt{3}] \text{R}30^\circ$ -type superlattice in Wood's notation, which means that $\text{LiNi}_{1/3}\text{Mn}_{1/3}\text{Co}_{1/3}\text{O}_2$ has a more stable structure than those of Li-stoichiometric unary transition-metal oxides. A series of micro-/nanoarchitected $\text{LiNi}_{1/3}\text{Mn}_{1/3}\text{Co}_{1/3}\text{O}_2$ samples were prepared to boost the electrochemical performance.^[43,44] Microspheres with many nanoparticles are the most common morphology for $\text{LiNi}_{1/3}\text{Mn}_{1/3}\text{Co}_{1/3}\text{O}_2$, which is usually synthesized via a two-step route. First, $(\text{Ni}_{1/3}\text{Co}_{1/3}\text{Mn}_{1/3})(\text{OH})_2$ or $\text{Ni}_{1/3}\text{Co}_{1/3}\text{Mn}_{1/3}\text{CO}_3$ is prepared, and then $(\text{Ni}_{1/3}\text{Co}_{1/3}\text{Mn}_{1/3})(\text{OH})_2$ or $\text{Ni}_{1/3}\text{Co}_{1/3}\text{Mn}_{1/3}\text{CO}_3$ reacts with Li salt to produce $\text{LiNi}_{1/3}\text{Mn}_{1/3}\text{Co}_{1/3}\text{O}_2$. Some hierarchical structures are fabricated via a template method. Cao and co-workers prepared $\text{LiNi}_{1/3}\text{Mn}_{1/3}\text{Co}_{1/3}\text{O}_2$ hollow microspheres assembled from nanoparticles ≈ 100 nm in size by using MnO_2 microspheres as a template.^[22] The micro/nanostructures delivered discharge capacities of 212 mA h g^{-1} at 0.1 C and 136 mA h g^{-1} at 10 C when cycling between 2.5 and 4.5 V. Coating with metal oxides is also an effective way to improve the electrochemical performance.^[45–47] Zhou and co-workers prepared ZrO_2 -coated $\text{LiNi}_{1/3}\text{Mn}_{1/3}\text{Co}_{1/3}\text{O}_2$ via a three-step route.^[45] $(\text{Ni}_{1/3}\text{Co}_{1/3}\text{Mn}_{1/3})(\text{OH})_2$ was first synthesized by the coprecipitation method, and it then was mixed with $\text{ZrO}(\text{NO}_3)_2$ to form ZrO_2 -coated $(\text{Ni}_{1/3}\text{Co}_{1/3}\text{Mn}_{1/3})(\text{OH})_2$ precursor. Finally, the precursor and Li_2CO_3 were mixed together and heated at 900°C . Compared with bare $\text{LiNi}_{1/3}\text{Mn}_{1/3}\text{Co}_{1/3}\text{O}_2$, 1 wt% ZrO_2 -coated

$\text{LiNi}_{1/3}\text{Mn}_{1/3}\text{Co}_{1/3}\text{O}_2$ showed better cycling and rate performance owing to suppression of the side reactions between the electrode and the electrolyte and the increase in the lattice parameters of the a and c axes.

Since it is very difficult to reach relatively satisfactory capacity with the Li-stoichiometric layered transition-metal oxides system, the Li-excess, layered transition-metal oxide $\text{Li}_2\text{MnO}_3\text{-LiNi}_{0.5}\text{Mn}_{0.5}\text{O}_2$ system (i.e., $x\text{Li}_2\text{MnO}_3 \cdot (1-x)\text{LiNi}_{0.5}\text{Mn}_{0.5}\text{O}_2$) has been proposed.^[48] $x\text{Li}_2\text{MnO}_3 \cdot (1-x)\text{LiNi}_{0.5}\text{Mn}_{0.5}\text{O}_2$ is composed of layered monoclinic Li_2MnO_3 with $\text{C}2/m$ symmetry and the layered $\text{LiNi}_{0.5}\text{Mn}_{0.5}\text{O}_2$ described above. $x\text{Li}_2\text{MnO}_3 \cdot (1-x)\text{LiNi}_{0.5}\text{Mn}_{0.5}\text{O}_2$ can deliver a high initial charge capacity of over 250 mA h g^{-1} , but it suffers from large irreversible capacity owing to the phase transformation during the initial cycles. To solve this problem, porous structures and surface modifications have been attempted.^[49–51] Our group synthesized nanoparticles assembled into porous $0.2\text{Li}_2\text{MnO}_3 \cdot 0.8\text{LiNi}_{0.5}\text{Mn}_{0.5}\text{O}_2$ nanorods (Figure 5a,b) via a solid-state reaction of LiOH , $\text{Ni}(\text{NO}_3)_2$, and porous Mn_2O_3 nanowires.^[50] A high initial discharge capacity of 275 mA h g^{-1} was obtained at 0.2 C , and capacity decay is only $\approx 10\%$ after 100 cycles (Figure 5c). The good cycling performance was attributed to two aspects: (1) the porous structure could accommodate the volume changes; (2) the nanostructure reduced the Li^+ diffusion paths. Apart from $x\text{Li}_2\text{MnO}_3 \cdot (1-x)\text{LiNi}_{0.5}\text{Mn}_{0.5}\text{O}_2$, $x\text{Li}_2\text{MnO}_3 \cdot (1-x)\text{LiMn}_{1/3}\text{Ni}_{1/3}\text{Co}_{1/3}\text{O}_2$ is frequently studied.^[52–55] Liu and Manthiram reported 1 wt% Al_2O_3 -coated and 1 wt% RuO_2 -coated $0.5\text{Li}_2\text{MnO}_3 \cdot 0.5\text{LiMn}_{1/3}\text{Ni}_{1/3}\text{Co}_{1/3}\text{O}_2$, which delivered a high capacity of 280 mA h g^{-1} at 0.05 C with capacity retention of 94.3% after 30 cycles.^[51] The Al_2O_3 layer suppressed O_2 release and the decomposition of the electrolyte, and the RuO_2 layer promoted electron transfer and Li^+ ion diffusion on the surface of the $0.5\text{Li}_2\text{MnO}_3 \cdot 0.5\text{LiMn}_{1/3}\text{Ni}_{1/3}\text{Co}_{1/3}\text{O}_2$. More recently, they have also designed a heterostructure composed of a Ni-rich $\text{LiNi}_{0.7}\text{Co}_{0.15}\text{Mn}_{0.15}\text{O}_2$ core and a Li-rich $\text{LiMn}_{1.2-x}\text{Ni}_{0.2}\text{Mn}_{0.6}\text{O}_2$ shell, which exhibited a discharge capacity of 190 mA h g^{-1} with high capacity retention of 98% and discharge-voltage retention of 97% during 100 cycles at $2.0\text{--}4.5 \text{ V}$ under the $\text{C}/3$ rate

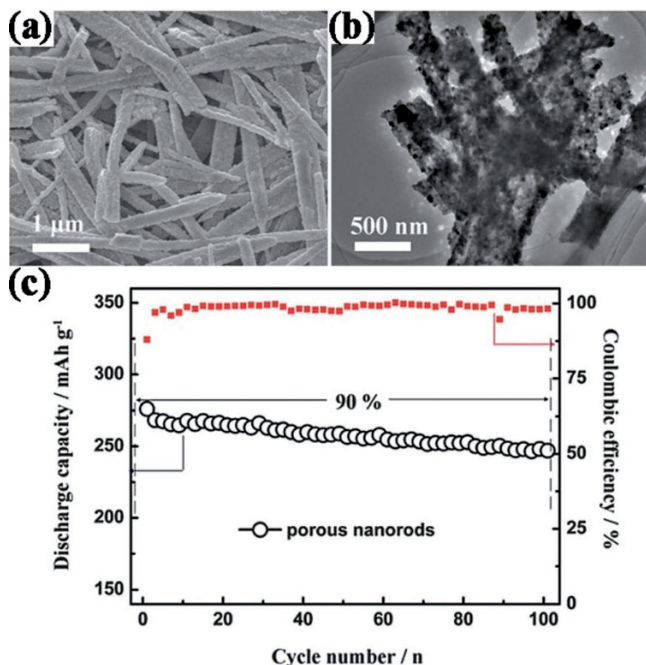


Figure 5. Scanning electron microscope (SEM) a) and transmission electron microscope (TEM) b) images of porous $0.2\text{Li}_2\text{MnO}_3 \cdot 0.8\text{LiNi}_{0.5}\text{Mn}_{0.5}\text{O}_2$ nanorods. c) Cycling performance of $0.2\text{Li}_2\text{MnO}_3 \cdot 0.8\text{LiNi}_{0.5}\text{Mn}_{0.5}\text{O}_2$ nanorods at 0.2 C between 2.0 and 4.8 V. Reproduced with permission.^[50] Copyright 2014, The Royal Society of Chemistry.

(1 C = 200 mA g⁻¹).^[56] This outstanding performance is attributed to the rational integration of the advantageous features of the structural stability of the core and the chemical stability of the shell, effectively addressing impedance rise and capacity fade stemming from the aggressive reaction between the cathode surface and the organic electrolyte at the higher operating voltages.

The high cost of Co resources, the Ni²⁺ which is exchanged into the Li slab, the Jahn-Teller effect of Mn³⁺, and O₂ release at high voltage are the main problems with the layered transition-metal oxides. $\text{LiNi}_{1/3}\text{Mn}_{1/3}\text{Co}_{1/3}\text{O}_2$, $\text{LiNi}_{0.8}\text{Co}_{0.15}\text{Al}_{0.05}\text{O}_2$, $\text{LiNi}_{0.8}\text{Co}_{0.1}\text{Mn}_{0.1}\text{O}_2$, and Li-excess $x\text{Li}_2\text{MnO}_3 \cdot (1-x)\text{LiNi}_{0.5}\text{Mn}_{0.5}\text{O}_2$, which are very promising for wide use in practical applications. Surface modification, micro/nanohierarchical structures, and core-shell or concentration-gradient structures can efficiently improve their rate and cycling performance. It is still difficult, however, to charge above 4.5 V and obtain a stable structure at high temperature. Therefore, Mn-based spinels with high working potential and polyanion-type compounds with high thermal stability are proposed.

2.2. Mn-Based Spinels

The spinel structure is usually represented by AB_2O_4 , in which O²⁻ ions form a cubic close packed structure, and A and B ions occupy the tetrahedral and octahedral sites,

respectively. For LIB cathode, Mn-based spinels mainly include LiMn_2O_4 and $\text{LiNi}_{0.5}\text{Mn}_{1.5}\text{O}_4$. Compared with layered transition metal oxides, the Mn-based spinels have less theoretical specific capacity but better rate performance, owing to their 3D Li⁺ ion diffusion channels, which make them ideal cathode materials for high power batteries.

2.2.1. LiMn_2O_4

Thackeray et al. discovered that spinel-type LiMn_2O_4 can achieve electrochemical Li⁺ extraction to form the $[\text{Mn}_2]\text{O}_4$ framework.^[57] In the subsequent 30 years, LiMn_2O_4 has been widely investigated as cathode for LIBs. LiMn_2O_4 features a cubic symmetry with $Fd\bar{3}m$ space group. The Li⁺, Mn^{3.5+} (average valence), and O²⁻ ions are located in the 8a, 16d, and 32e sites, respectively. The edge-sharing MnO₆ octahedra in LiMn_2O_4 form a continuous 3D cubic array, leading to a robust spinel framework. The LiO₄ tetrahedra share each face with adjacent vacant 16c octahedra. During cycling, the Li⁺ ions could diffuse from one 8a site into another 8a site via neighbouring 16c site to form a 3D path.^[58] LiMn_2O_4 possesses a ≈4 V redox potential based on a two-step reaction ($\text{LiMn}_2\text{O}_4/\text{Li}_{0.5}\text{Mn}_2\text{O}_4$ and $\text{Li}_{0.5}\text{Mn}_2\text{O}_4/\lambda\text{-MnO}_2$) with an ≈0.15 V voltage difference. If discharged to 3 V, rock-salt structured $\text{Li}_2\text{Mn}_2\text{O}_4$ is formed, causing severe Jahn-Teller distortion from the cubic to the tetragonal phase, so over-discharge leads to poor cycling performance. Furthermore, the side reaction of $2\text{Mn}^{3+} \rightarrow \text{Mn}^{2+} + \text{Mn}^{4+}$ results in Mn dissolution, which is also destructive to cycling stability, especially at high temperature (>40 °C).^[59,60]

Strategies to improve the cycling stability of LiMn_2O_4 mainly include modifying the surface, preparing porous or hollow structures, and synthesizing LiMn_2O_4 /carbon composites.^[61–66] Cho and co-workers fabricated 5 wt% $\text{LiNi}_{0.5}\text{Mn}_{0.5}\text{O}_2$ -coated LiMn_2O_4 via a spray-drying process, and the heterostructured LiMn_2O_4 delivered a discharge capacity of 123 mAh g⁻¹ with capacity retention of 85% at 60 °C after 100 cycles.^[61] The stable surface reduces the side reactions and provides efficient Li⁺ diffusion paths. Our group prepared porous LiMn_2O_4 nanorods through a solid state reaction of porous Mn_2O_3 nanorods and LiOH.^[63] Figure 6 shows a scanning electron microscope (SEM) image, a transmission electron microscope (TEM) image, and the cycling performance of porous LiMn_2O_4 nanorods consisting of aggregated nanoparticles. The capacity retention of

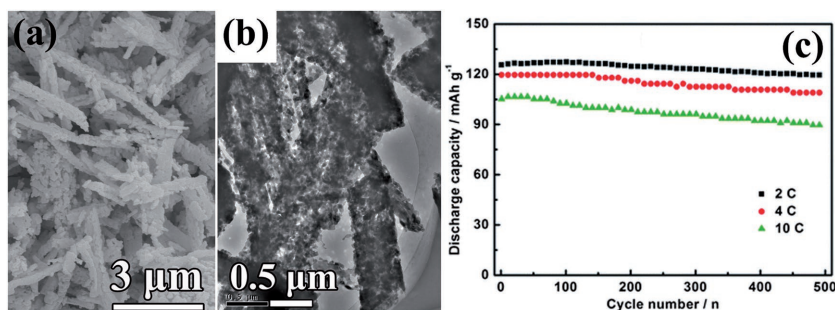


Figure 6. a) SEM image, b) TEM image, and c) cycling performance of the porous LiMn_2O_4 nanorods at different discharge rates. Reproduced with permission.^[63] Copyright 2011, The Royal Society of Chemistry.

porous LiMn_2O_4 nanorods approached 90% after 500 cycles at 2 C, which indicated that the 1D porous nanostructure not only has large specific surface area to allow efficient active mass-electrolyte contact, but also provides 1D electron transport pathways. Bak et al. prepared $\text{LiMn}_2\text{O}_4/\text{reduced graphene oxide (rGO)}$ nanocomposites by the microwave-assisted hydrothermal method.^[64] The $\text{LiMn}_2\text{O}_4/\text{rGO}$ exhibited high specific capacities of 137 mAh g^{-1} at 1 C, 117 mAh g^{-1} at 50 C, and 101 mAh g^{-1} at 100 C, as well as excellent capacity retention of 90% at 1 C and 96% at 10 C after 100 cycles. The highly conductive rGO and highly crystalline LiMn_2O_4 nanoparticles synergistically enhanced the electrochemical performance.

2.2.2. $\text{LiNi}_{0.5}\text{Mn}_{1.5}\text{O}_4$

Spinel-type $\text{LiNi}_{0.5}\text{Mn}_{1.5}\text{O}_4$ can act as Ni-doped LiMn_2O_4 , which contains Ni^{2+} and Mn^{4+} ions, eliminating the Jahn-Teller distortion. $\text{LiNi}_{0.5}\text{Mn}_{1.5}\text{O}_4$ has a high redox potential of 4.7 V based on $\text{Ni}^{4+}/\text{Ni}^{3+}$ and $\text{Ni}^{3+}/\text{Ni}^{2+}$ couples.^[67] $\text{LiNi}_{0.5}\text{Mn}_{1.5}\text{O}_4$ has two sorts of crystal structure: ordered $P4_332$ phase and disordered $Fd\bar{3}m$ phase.^[68] In $Fd\bar{3}m$ phase, Ni^{2+} and Mn^{4+} ions are located in half of the octahedral sites (16d), and Li^+ ions occupy an eighth of the tetrahedral sites (8a) (Figure 7a). In $P4_332$ phase, Li^+ , Ni^{2+} , and Mn^{4+} ions are located in the 8a, 4b, and 12d sites, respectively, while O ions occupy the 8c and 24e sites (Figure 7b). The nanosized $\text{LiNi}_{0.5}\text{Mn}_{1.5}\text{O}_4$ with $Fd\bar{3}m$ phase favors high-rate capability, while the microsized $\text{LiNi}_{0.5}\text{Mn}_{1.5}\text{O}_4$ with $P4_332$ phase is of benefit for long-term cyclability. Considering both phase and size effects, hierarchical structured $\text{LiNi}_{0.5}\text{Mn}_{1.5}\text{O}_4$ is promising.

Lou and co-workers designed and prepared hollow $\text{LiNi}_{0.5}\text{Mn}_{1.5}\text{O}_4$ spheres and cubes assembled from nanoparticles via a solid-state reaction using porous MnO_2 spheres and cubes as precursors, and the hollow structures delivered discharge capacities of 118 mAh g^{-1} at 1 C and 104 mAh g^{-1} at 20 C.^[69] The hollow micro-/nanostructure provides short Li^+ diffusion distances and large contact area between the electrode and electrolyte, leading to high rate capability. Sun and co-workers synthesized core-shell structured $\text{Li}[(\text{Li}_{0.05}\text{Mn}_{0.95})_{0.8}(\text{Ni}_{0.25}\text{Mn}_{0.75})_{0.2}]_2\text{O}_4$ through core-shell structured $\text{MnCO}_3-(\text{Ni}_{0.25}\text{Mn}_{0.75})\text{CO}_3$ precursor, and capacity retention of 97% was obtained after 100 cycles at 60 °C.^[70] Our group constructed and explored porous $\text{LiNi}_{0.5}\text{Mn}_{1.5}\text{O}_4$ nanorods that were prepared via a solid-state reaction using porous Mn_2O_3 nanowires/rods as the templates.^[71] The

porous $\text{LiNi}_{0.5}\text{Mn}_{1.5}\text{O}_4$ nanorods were composed of interconnected nanosized particles (Figure 8a,b). Combining the cycling stability of $P4_332$ phase structure with the fast Li^+ diffusion of porous nanomaterials, the porous $\text{LiNi}_{0.5}\text{Mn}_{1.5}\text{O}_4$ nanorods achieved 91% capacity retention after 500 cycles at 5 C. Compared with bulk materials, the 1D porous nanostructures accommodated the strain caused by lattice variation during Li insertion/extraction and maintained the structural integrity of the material (Figure 8c). Our group also synthesized micro/nano hierarchically structured $\text{LiNi}_{0.5}\text{Mn}_{1.5}\text{O}_4$ with high tap density of 1.7 g cm^{-3} via a facile polyethylene glycol (PEG)-assisted coprecipitation method.^[72] Its discharge capacity at 40 C was more than 120 mAh g^{-1} , and the capacity retention at 5 C reached 89% after 150 cycles. These results suggest that developing hierarchical micro/nanostructured $\text{LiNi}_{0.5}\text{Mn}_{1.5}\text{O}_4$ is an effective way to develop $\text{LiNi}_{0.5}\text{Mn}_{1.5}\text{O}_4$. In order to increase the capacity of spinel lithium nickel manganese oxide (LNMO), LNMO/layered lithiated 3d-transition metal oxide heterostructures are proposed. Our group synthesized intergrown $0.5\text{LiNi}_{1/3}\text{Mn}_{1/3}\text{Co}_{1/3}\text{O}_2 \cdot 0.5\text{LiNi}_{0.5}\text{Mn}_{1.5}\text{O}_4$ nanorods via a solid-state reaction using $\beta\text{-MnO}_2$ nanorods as a self-support template.^[73] The composite delivered the highest discharge capacity of 200 mAh g^{-1} at 0.1 C. The capacity retention of 87% was achieved after 100 cycles at 0.2 C. $0.5\text{LiNi}_{1/3}\text{Mn}_{1/3}\text{Co}_{1/3}\text{O}_2 \cdot 0.5\text{LiNi}_{0.5}\text{Mn}_{1.5}\text{O}_4$, integrating the advantages of high-capacity $\text{LiNi}_{1/3}\text{Mn}_{1/3}\text{Co}_{1/3}\text{O}_2$ and high-voltage $\text{LiNi}_{0.5}\text{Mn}_{1.5}\text{O}_4$, is a potential candidate for LIBs with high energy.

Mn-based spinels feature low cost and environmental friendliness. Through designing hollow or porous structures, the capacity, rate capability, and cycling stability of spinel-type Mn-based oxides are all obviously improved, benefitting from the fast Li^+ diffusion paths. Significantly, Mn-based spinels (i.e., $\text{LiNi}_{0.5}\text{Mn}_{1.5}\text{O}_4$) possess the relatively high redox potential of $\approx 4.7 \text{ V}$, making them very promising high-potential cathode materials. It is difficult, however, to find a stable electrolyte when charging over 5.0 V. Therefore, avoiding overcharge and exploring safe electrolytes is very important for Mn-based spinels.

2.3. Polyanion-Type Compounds

Polyanion-type compounds mainly include olivine-type LiMPO_4 ($M = \text{Fe}, \text{Mn}, \text{Co}, \text{and Ni}$), sodium superionic conductor (NASICON)-type $\text{Li}_3\text{V}_2(\text{PO}_4)_3$, and silicate-based Li_2MSiO_4 ($M = \text{Fe}, \text{Mn}, \text{and Co}$). Compared with layered lithiated transition-metal oxides, polyanion-type compounds feature higher thermal stability and better safety owing to the stronger covalent bonds of O^{2-} ions. Moreover, polyanion-type compounds have higher theoretical specific capacities than those of Mn-based spinels. Nevertheless, polyanion-type compounds suffer from poor electronic and ionic conductivities, leading to poor rate performance. Carbon-coating combined with nanostructures is an effective strategy to solve this problem.

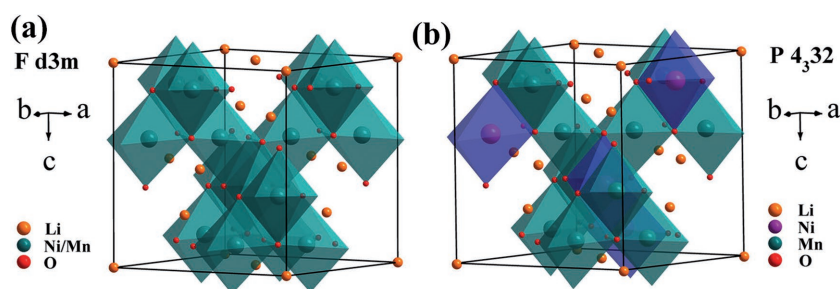


Figure 7. Crystal structures of $\text{LiNi}_{0.5}\text{Mn}_{1.5}\text{O}_4$ with disordered $Fd\bar{3}m$ phase a) and ordered $P4_332$ phase b). Reproduced with permission.^[68] Copyright 2013, Springer Berlin Heidelberg.

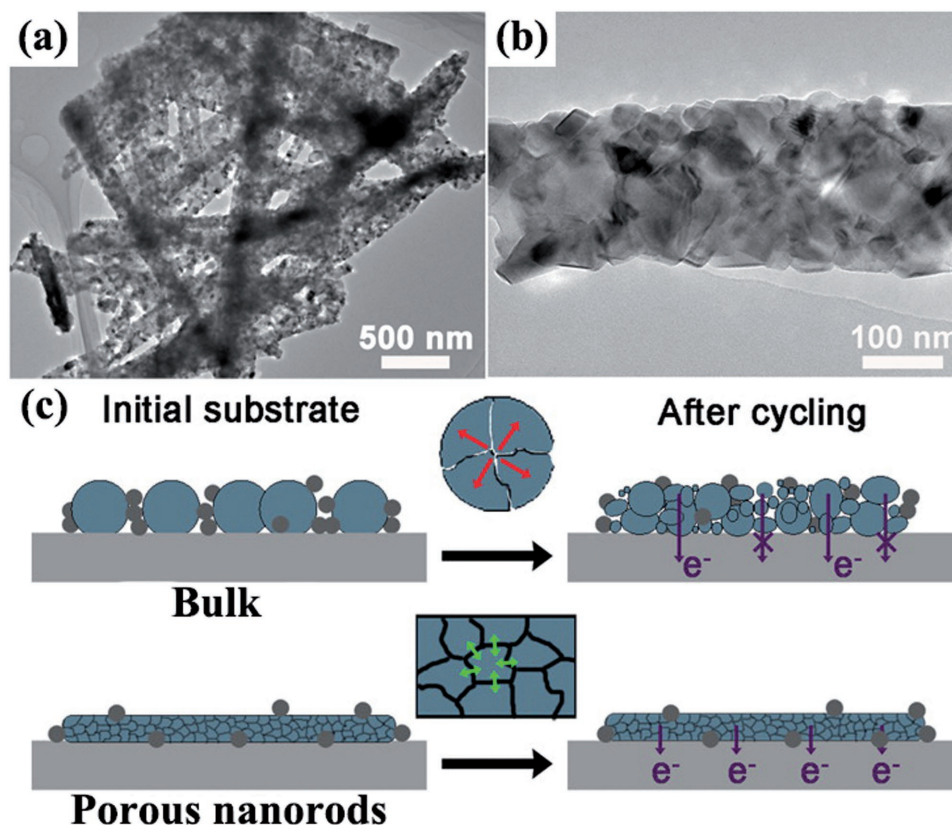


Figure 8. a,b) TEM images of porous $\text{LiNi}_{0.5}\text{Mn}_{1.5}\text{O}_4$ nanorods. c) Schematic illustration of morphology change and electron transportation in bulk $\text{LiNi}_{0.5}\text{Mn}_{1.5}\text{O}_4$ and porous $\text{LiNi}_{0.5}\text{Mn}_{1.5}\text{O}_4$ nanorods during electrochemical cycling. Reproduced with permission.^[71] Copyright 2013, American Chemical Society.

2.3.1. Olivine-Type LiMPO_4

The olivine LiMPO_4 as a cathode for LIBs was first reported by Goodenough and co-workers.^[74] LiMPO_4 possesses an orthorhombic symmetry with $Pnma$ space group, in which the O^{2-} ions have a hexagonal close-packed (hcp) structure, Li^+ and M^{2+} ions occupy half of the octahedral sites, and P^{5+} ions occupy 1/8 of the tetrahedral sites (Figure 9a). Li^+ ions diffuse along the 1D [010] direction (i.e., the b -axis) during cycling. LiFePO_4 , LiMnPO_4 , LiCoPO_4 , and LiNiPO_4 have redox potentials of 3.45, 4.1, 4.8, and 5.1 V, respectively (Figure 9b). It is difficult to meet the high potentials of LiCoPO_4 and LiNiPO_4 with the commonly used electrolytes. This is the reason why most reports focus on LiFePO_4 and LiMnPO_4 .

LiFePO_4 has a theoretical specific capacity of 170 mAh g^{-1} based on the $\text{Fe}^{3+}/\text{Fe}^{2+}$ couple and features only slight volume change (6.81%) during the charge-discharge process, but it suffers from low intrinsic electronic conductivity ($\approx 10^{-9} \text{ S cm}^{-1}$).^[75–78] A series of nanostructured LiFePO_4 samples with carbon coating were created to solve this problem.^[79–85] Zhou and co-workers designed and prepared a core-shell-structured LiFePO_4/C nanocomposite via an in situ polymerization restriction method using $\text{FePO}_4/\text{polyaniline}$ precursor.^[80] The composite had a particle size of 20–40 nm with a carbon layer thickness of 1–2 nm, which delivered a capacity of 90 mAh g^{-1} at 10 A g^{-1} (58.8 C) and had less than 5% capacity loss after

1100 cycles at 0.1 A g^{-1} . The nanosized LiFePO_4 combined with a complete coating of carbon showed effectively enhanced its electronic transport and ionic diffusion. Guo and co-workers reported double nanocarbon (amorphous carbon and graphitized carbon nanotubes (CNTs)) modified LiFePO_4 nanoparticles, which were synthesized via a polyol route combined with a carbon-coating procedure.^[83] The nanocomposite could achieve a discharge capacity of 94.4 mAh g^{-1} with capacity retention of 98.5% after 500 cycles at an ultrahigh rate of 120 C. The excellent performance was attributed to the synergistic function of the amorphous carbon and graphitized CNTs. The amorphous carbon which homogeneously encapsulated all LiFePO_4 nanoparticles promoted Li^+ diffusion and stabilized the interface between the LiFePO_4 and the electrolyte. Meanwhile, the CNTs decreased the internal impedance and formed a 3D conducting network extending through the whole electrode. Mo et al. fabricated a 3D $\text{LiFePO}_4/\text{rGO}$ composite assembled layer-by-layer by the solvothermal method.^[84] The $\text{LiFePO}_4/\text{rGO}$ composite displayed discharge capacities of 146, 121, 81, and 56 mAh g^{-1} at 1, 10, 80, and 160 C, respectively. The layer-by-layer assembled structure enabled fast Li^+ transport, and the rGO improved the electronic conductivity.

LiMnPO_4 possesses a similar theoretical specific capacity of 171 mAh g^{-1} based on the reaction of $\text{LiMnPO}_4 \leftrightarrow \text{MnPO}_4 + \text{Li}^+ + \text{e}^-$, while it has a higher redox potential (4.1 V) than LiFePO_4 , which enhances the energy density.^[86,87] LiMnPO_4 has lower

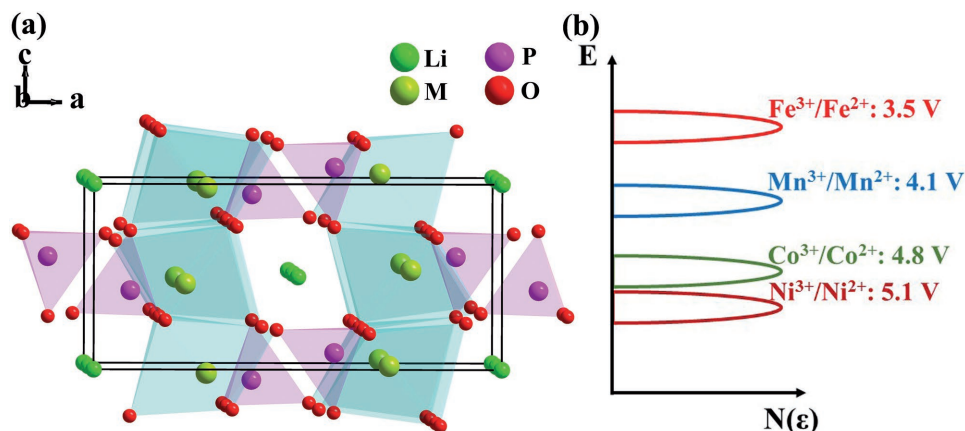


Figure 9. Crystal structure a) and schematic illustration of the electronic structure b) of LiMPO_4 ($M = \text{Fe, Mn, Co, and Ni}$).

electronic conductivity (less than $10^{-10} \text{ S cm}^{-1}$), however, and larger volume changes (9.5%) compared with LiFePO_4 . In addition, the structural distortion induced by the Jahn-Teller effect of Mn^{3+} ions leads to low practical capacity. Preparing nanostructured LiMnPO_4 with a uniform carbon coating is also an effective way to solve these problems.^[87,88] Cho and co-workers prepared ultrafine LiMnPO_4 particles ($\approx 6 \text{ nm}$) embedded in 3D macroporous carbon flakes by using polymethylmethacrylate (PMMA) as the template.^[88] The flakes delivered discharge capacities of 162 mAh g^{-1} at 0.1 C and 110 mAh g^{-1} at 10 C . Choi et al. synthesized porous LiMnPO_4/C nanoplates via a solid-state reaction.^[89] The porous nanoplates were assembled from many nanorods growing along the Li^+ diffusion direction, which promoted the two-phase reaction of LiMnPO_4 .

The discharge capacities reached 168 mAh g^{-1} at 0.02 C and 117 mAh g^{-1} at 1 C .

In addition to LiFePO_4 and LiMnPO_4 , $\text{LiFe}_x\text{Mn}_{1-x}\text{PO}_4$ is also a promising cathode material which combines the high potential of LiMnPO_4 and the high stability of LiFePO_4 .^[90–95] Cui and co-workers manufactured single-crystalline $\text{LiMn}_{0.75}\text{Fe}_{0.25}\text{PO}_4$ nanorods anchored in rGO by the solvothermal method.^[91] The composite presented high electronic conductivity ($0.1\text{--}1 \text{ S cm}^{-1}$) and excellent rate capability (155 mAh g^{-1} at 0.5 C and 132 mAh g^{-1} at 20 C). Scrosati and co-workers prepared carbon-coated core-shell structured $\text{LiMn}_{0.85}\text{Fe}_{0.15}\text{PO}_4\text{-LiFePO}_4$ through a two-step precipitation route followed by a two-step heat treatment (Figure 10).^[93] The $\text{LiMn}_{0.85}\text{Fe}_{0.15}\text{PO}_4\text{-LiFePO}_4/\text{C}$ composite presented a nanoporous microspherical

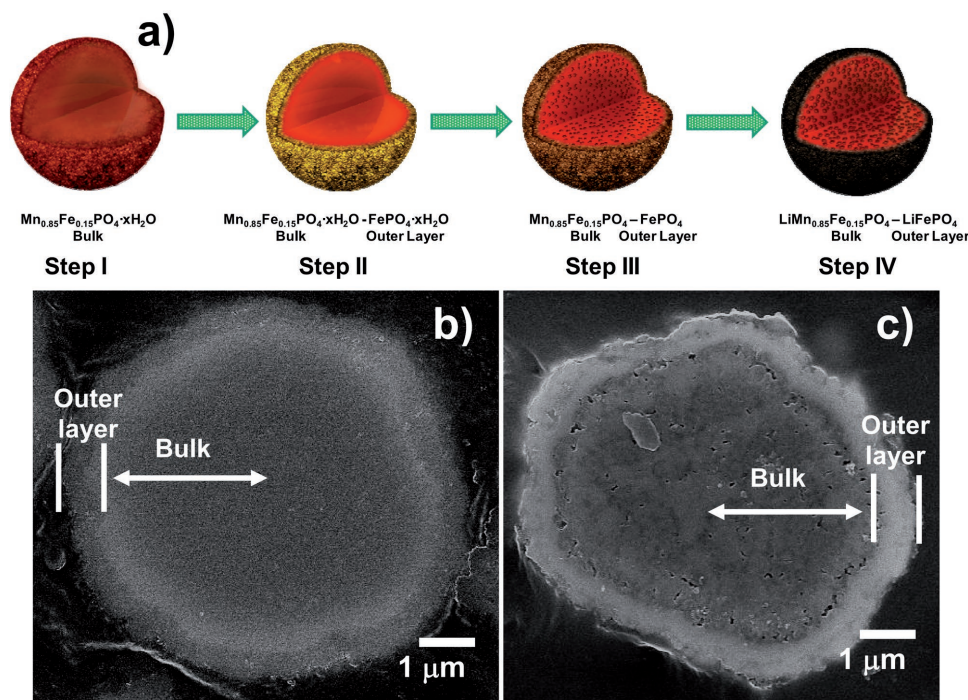


Figure 10. a) Formation procedure for double-structured micron-sized $\text{LiMn}_{0.85}\text{Fe}_{0.15}\text{PO}_4\text{-LiFePO}_4/\text{C}$ composite; SEM cross-sectional images of b) $\text{Mn}_{0.85}\text{Fe}_{0.15}\text{PO}_4\text{-FePO}_4$ composite and c) $\text{LiMn}_{0.85}\text{Fe}_{0.15}\text{PO}_4\text{-LiFePO}_4/\text{C}$ composite. Reproduced with permission.^[93] Copyright 2012, WILEY-VCH.

morphology and displayed a high tap density of 1.5 g cm^{-3} . The volumetric specific capacity reached 240 mAh cm^{-3} at 0.5 C , and capacity retention of 97% was achieved after 50 cycles.

2.3.2. NASICON-Type $\text{Li}_3\text{V}_2(\text{PO}_4)_3$

$\text{Li}_3\text{V}_2(\text{PO}_4)_3$ features a high theoretical capacity of 197 mAh g^{-1} based on the $3e^-$ reaction in the voltage range from 3.0 to 4.8 V.^[96–98] During the charge process, $\text{Li}_3\text{V}_2(\text{PO}_4)_3$ first turns into $\text{Li}_{2.5}\text{V}_2(\text{PO}_4)_3$ ($\approx 3.7 \text{ V}$) and then becomes $\text{Li}_2\text{V}_2(\text{PO}_4)_3$ ($\approx 3.8 \text{ V}$) with V^{3+} transformed to a mixture of V^{3+} and V^{4+} . On further deintercalating Li^+ ions, the $\text{Li}_2\text{V}_2(\text{PO}_4)_3$ is successively transformed into $\text{LiV}_2(\text{PO}_4)_3$ ($\approx 4.1 \text{ V}$) and $\text{V}_2(\text{PO}_4)_3$ ($\approx 4.6 \text{ V}$) based on the $\text{V}^{4+}/\text{V}^{3+}$ and $\text{V}^{5+}/\text{V}^{4+}$ couples. In the discharge, $\text{V}_2(\text{PO}_4)_3$ first changes to $\text{Li}_2\text{V}_2(\text{PO}_4)_3$ with an inclined platform from 4.0 to 3.6 V, and then $\text{Li}_{2.5}\text{V}_2(\text{PO}_4)_3$ and $\text{Li}_3\text{V}_2(\text{PO}_4)_3$ are formed at ≈ 3.6 and $\approx 3.5 \text{ V}$, respectively. Because $\text{V}_2(\text{PO}_4)_3$ has an unstable structure, most studies control the voltage range to between 3.0 and 4.3 V, which makes the $2e^-$ reaction occur with a capacity of 132 mAh g^{-1} .^[99,100]

Though $\text{Li}_3\text{V}_2(\text{PO}_4)_3$ possesses a higher electronic conductivity ($\approx 10^{-7} \text{ S cm}^{-1}$) than those of LiFePO_4 and LiMnPO_4 ,^[101] the value is still low, which severely limits its power density. Some $\text{Li}_3\text{V}_2(\text{PO}_4)_3/\text{C}$ composites are reported to improve the kinetics. Li et al. synthesized 3D ordered macroporous $\text{Li}_3\text{V}_2(\text{PO}_4)_3/\text{C}$ nanocomposite by using PMMA as the template.^[102] The composite showed discharge capacities of $\approx 156 \text{ mAh g}^{-1}$ at 0.1 C and 70 mAh g^{-1} at 20 C . Zhu et al. prepared $\text{Li}_3\text{V}_2(\text{PO}_4)_3/\text{rGO}$ nanocomposite via a rheological method with a following heat treatment, and the composite delivered high rate capability (142 mAh g^{-1} at 0.075 C and 119 mAh g^{-1} at 15 C).^[101] Mai and co-workers fabricated bicontinuous hierarchical $\text{Li}_3\text{V}_2(\text{PO}_4)_3/\text{C}$ mesoporous nanowires through hydrothermal and annealing treatments.^[103] The in situ crystallization and carbonization

processes are beneficial for the nanocrystals embedded in the conductive scaffold, which conducive to effective electron contact. The hierarchical structure endows the $\text{Li}_3\text{V}_2(\text{PO}_4)_3/\text{C}$ nanowires with enhanced rate capability and cycling stability. When cycled between 3.0 and 4.3 V, the composite achieved high-rate capability and ultralong-term cyclability (capacity retention of 80.0% after 3000 cycles) (Figure 11). Also, Mai and co-workers proposed a feasible one-pot method to prepare hierarchical carbon decorated $\text{Li}_3\text{V}_2(\text{PO}_4)_3$, achieving enhanced rate capability (121 mAh g^{-1} at 30 C), superior cycling stability (77% retention after 4000 cycles at 20 C), and excellent temperature adaptability (130 mAh g^{-1} at 20 C and $60 \text{ }^\circ\text{C}$, 106 mAh g^{-1} at 5 C and $-20 \text{ }^\circ\text{C}$).^[104] There are an electrolyte-filled macro/mesopore network and a buffered protective carbon shell in the unique hierarchical architecture, favorable for continuous electron conduction and rapid ion transport.

2.3.3. Silicate-Based Li_2MSiO_4

Li_2MSiO_4 ($\text{M} = \text{Fe}$) cathode was first reported by Nyttén et al. in 2005.^[105] Li_2MSiO_4 has various crystal structures, which are mainly classified into four space groups: $P2_1/n$, $Pmn2_1$, Pn , and $Pmnb$. All the crystal structures consist of tetrahedral units of LiO_4 , FeO_4 , and SiO_4 . All the $\text{Li}_2\text{FeSiO}_4$, $\text{Li}_2\text{MnSiO}_4$, and $\text{Li}_2\text{CoSiO}_4$ samples have two-step Li^+ insertion/deinsertion with redox potentials of 2.8/4.8, 4.1/4.5, and 4.2/5.0 V, respectively. It is very difficult to extract the second Li^+ from $\text{Li}_2\text{CoSiO}_4$ due to the limited stability of the electrolyte, and the structure of LiCoSiO_4 is also unstable. Therefore, most reports are focused on $\text{Li}_2\text{FeSiO}_4$ and $\text{Li}_2\text{MnSiO}_4$.

$\text{Li}_2\text{FeSiO}_4$ features environmental friendliness and low price, and it also has a high theoretical specific capacity of 332 mAh g^{-1} based on a $2e^-$ reaction.^[106,107] Nevertheless, $\text{Li}_2\text{FeSiO}_4$ is plagued by inferior electronic conductivity ($\approx 10^{-16} \text{ S cm}^{-1}$)

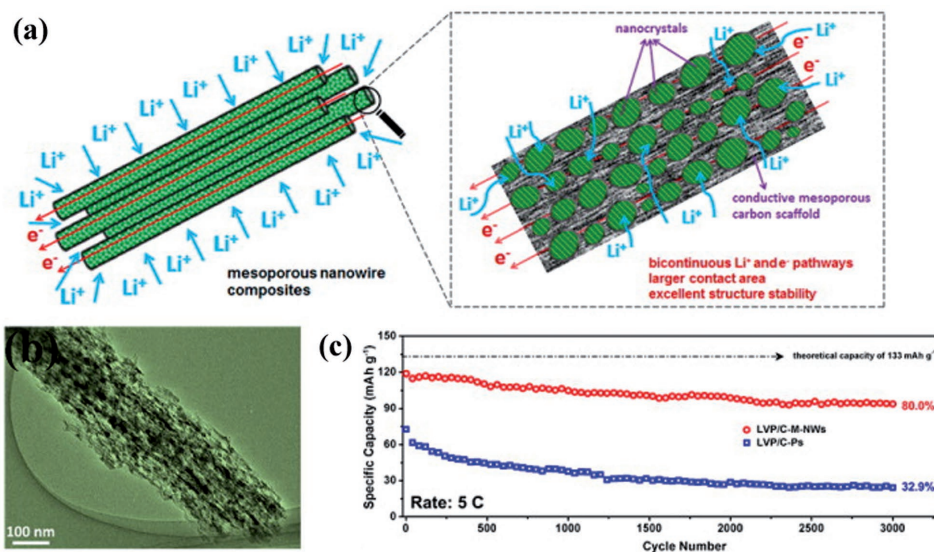


Figure 11. a) Schematic illustration of mesoporous nanowire composite with bicontinuous electron/ion transport pathways, large electrode–electrolyte contact area, and facile strain relaxation during Li^+ extraction/insertion. b) TEM images of $\text{Li}_3\text{V}_2(\text{PO}_4)_3/\text{C}$ mesoporous nanowire. c) Ultralong-life cycling performance of the $\text{Li}_3\text{V}_2(\text{PO}_4)_3/\text{C}$ mesoporous nanowires and $\text{Li}_3\text{V}_2(\text{PO}_4)_3/\text{C}$ particles at 5 C . Reproduced with permission.^[103] Copyright 2014, American Chemical Society.

and a low Li^+ ion diffusion coefficient, which severely limit its rate performance.^[17] In addition, it is hard to achieve multiple e^- reactions at room temperature because of the unstable Fe^{4+} . Carbon coating is the most effective way to not only enhance the kinetics, but also avoid the oxidation of Fe^{2+} .^[106,108–110] Our group synthesized spindle-like $\text{Li}_2\text{FeSiO}_4$ through hydrothermal synthesis, and then coated the $\text{Li}_2\text{FeSiO}_4$ using glucose as the carbon source to produce a $\text{Li}_2\text{FeSiO}_4@\text{C}$ nanocomposite.^[106] The composite with 7.21 wt% carbon showed a discharge capacity of 213 mAh g^{-1} ($\approx 1.28 e^-$) at 45 °C and 0.1 C. Zhu et al. reported 3D macroporous $\text{Li}_2\text{FeSiO}_4$ /graphene composite synthesized by a solution method using poly(ethylene glycol)-*block*-poly-(propylene glycol)-*block*-poly(ethylene glycol) P123 ($\text{EO}_{20}\text{PO}_{70}\text{EO}_{20}$) as a soft template.^[108] Because of the porous 3D conductive network, the composite displayed discharge capacities of 313 mAh g^{-1} at 0.1 C and 45 mAh g^{-1} at 50 C. Intergrown $(1-x)\text{Li}_2\text{FeSiO}_4 \cdot x\text{LiFePO}_4$ was also used to enable $\text{Li}_2\text{FeSiO}_4$ to deintercalate more Li^+ ions. Our group synthesized $0.96\text{Li}_2\text{FeSiO}_4 \cdot 0.04\text{LiFePO}_4@\text{C}$ by a sol-gel route.^[111] The LiFePO_4 additive effectively reduced the charge transfer resistance and apparent activation energy. The composite material showed enhanced capacities of 209 mAh g^{-1} at 15 °C and 284.7 mAh g^{-1} at 45 °C at 0.2 C.

$\text{Li}_2\text{MnSiO}_4$ also possesses the high theoretical capacity of 333 mAh g^{-1} based on $\text{Mn}^{3+}/\text{Mn}^{2+}$ and $\text{Mn}^{4+}/\text{Mn}^{3+}$ couples, but it suffers from low intrinsic electronic conductivity (6×10^{-14} S cm^{-1}). Furthermore, $\text{Li}_2\text{MnSiO}_4$ undergoes a gradual decrease in its crystallinity during cycling owing to the position exchange between Li and Mn. Carbon coating, as well as decreasing the particle size, can obviously promote the electronic conductivity and Li^+ ion diffusion coefficient.^[112–116] Yang and co-workers reported a $\text{Li}_2\text{MnSiO}_4/\text{C}$ nanocomposite with a discharge capacity of 209 mAh g^{-1} at 5 mA g^{-1} , which first material to achieve a reaction of more than one e^- among the silicate cathode materials.^[113] He and Manthiram prepared hierarchically macro/mesoporous $\text{Li}_2\text{MnSiO}_4/\text{C}$ nanocomposite by using PMMA as a template, and the composite delivered a discharge capacity of 200 mAh g^{-1} at 0.1 C at 45 °C.^[115] Our group synthesized core-shell structured $\text{Li}_2\text{MnSiO}_4@\text{C}$ nanoparticles by a hydrothermally assisted solution method.^[117] The composite presented 5.15 wt% carbon content and an average particle size of 22.8 nm. The discharge capacities of the composite were 282 mAh g^{-1} at 0.05 C and 103.4 mAh g^{-1} at 5 C.

LiFePO_4 has been successfully applied in automobile batteries, and other polyanion-type compounds have also been widely explored and investigated. All polyanion-type compounds have a stable framework, but they suffer from low intrinsic electronic conductivity and low Li^+ ion diffusion coefficients, leading to sluggish kinetics. Proper design of the hierarchical structure through particle-downsizing and carbon-coating, and micro/nano self-assembly can efficiently enhance their cycling and rate performance. $\text{Li}_2\text{FeSiO}_4$ and $\text{Li}_2\text{MnSiO}_4$ provide feasibility for achieving multiple e^- reactions per formula unit. Although there are still problems, the combination of phosphates and silicates is a promising choice that is worth attempting.

In this section, many new-type cathode materials along with the traditional ones with hierarchical structures all have

been reviewed. Ni-rich layered oxides, Mn-based spinels, and olivine-type phosphates are three promising materials. Ni-rich layered oxides possess high capacity and 2D Li^+ diffusion paths, but they suffer from cation disorder and O_2 release. Modifying the surface with oxides and preparing the core-shell structure with a highly stable shell can obviously improve the cycling performance and partially promote Li^+ transport. Mn-based spinels have a high working voltage and 3D Li^+ diffusion paths, but they are impeded by their low theoretical specific capacities. Intergrown layered oxide/Mn-based spinel with 1D porous structure enhances the specific energy. Olivine-type phosphates possess high stability but are plagued by sluggish kinetics. Carbon-coating combined with downsizing and porous design can boost the electronic conductivity and shorten the Li^+ diffusion paths. Research progress on cathode materials will further enhance the energy density, such as by preparing Li-excess layered oxides/ $\text{LiNi}_{0.5}\text{Mn}_{1.5}\text{O}_4$ composites with hierarchical structure.

3. Anode Materials

Most anode materials have higher capacity than cathode materials. They can be divided into three categories, depending on the reaction mechanism that occurs in the charge/discharge process: insertion reaction (e.g., 6C (graphite) + $\text{Li} \leftrightarrow \text{LiC}_6$), alloying reaction (e.g., $\text{Sn} + 4.4\text{Li} \leftrightarrow \text{Li}_{4.4}\text{Sn}$), and conversion reaction (e.g., $\text{Fe}_2\text{O}_3 + 6\text{Li} \leftrightarrow 2\text{Fe} + 3\text{Li}_2\text{O}$) (Figure 12).^[118] Insertion-type materials rely on the diffusion of Li^+ into the interspaces of a layer-structured anode, forming a sandwich-like architecture; they have good cycling ability, but relative low capacity. In contrast, alloying- and conversion-type materials carry on the actual redox reaction and exhibit relatively high capacity, but they suffer from large volume changes. Furthermore, some oxides and sulfides intrinsically possess low electronic conductivity, leading to poor rate performance. Designing a hierarchical structure is a typical scheme to solve these problems. First, a hierarchical structure provides a large surface area to greatly increase the contact area between electrode and electrolyte, which is favorable for the infiltration of electrolyte. Second, it shortens the ion diffusion distance as well as the electron transport pathways to allow for rapid diffusion kinetics. Third, the hierarchical structure offers more space to adapt to the volume changes and to some extent maintain the structural stability. All these will undoubtedly contribute to outstanding lithium storage performance.

3.1. Insertion-Type Materials

Insertion-type materials mainly include carbon materials and spinel-type $\text{Li}_4\text{Ti}_5\text{O}_{12}$. Graphite, as the commercial LIB anode material, has a relatively low theoretical discharge capacity of 372 mAh g^{-1} . The rate performance of graphite is not satisfactory, however, due to the slow diffusion rate of Li^+ . In addition, the low potential of Li^+ insertion promotes the formation of lithium dendrites and the dissolution of electrolyte, which are unfavorable factors in practical application. In the case of other porous carbon materials, Li^+ ions first insert themselves

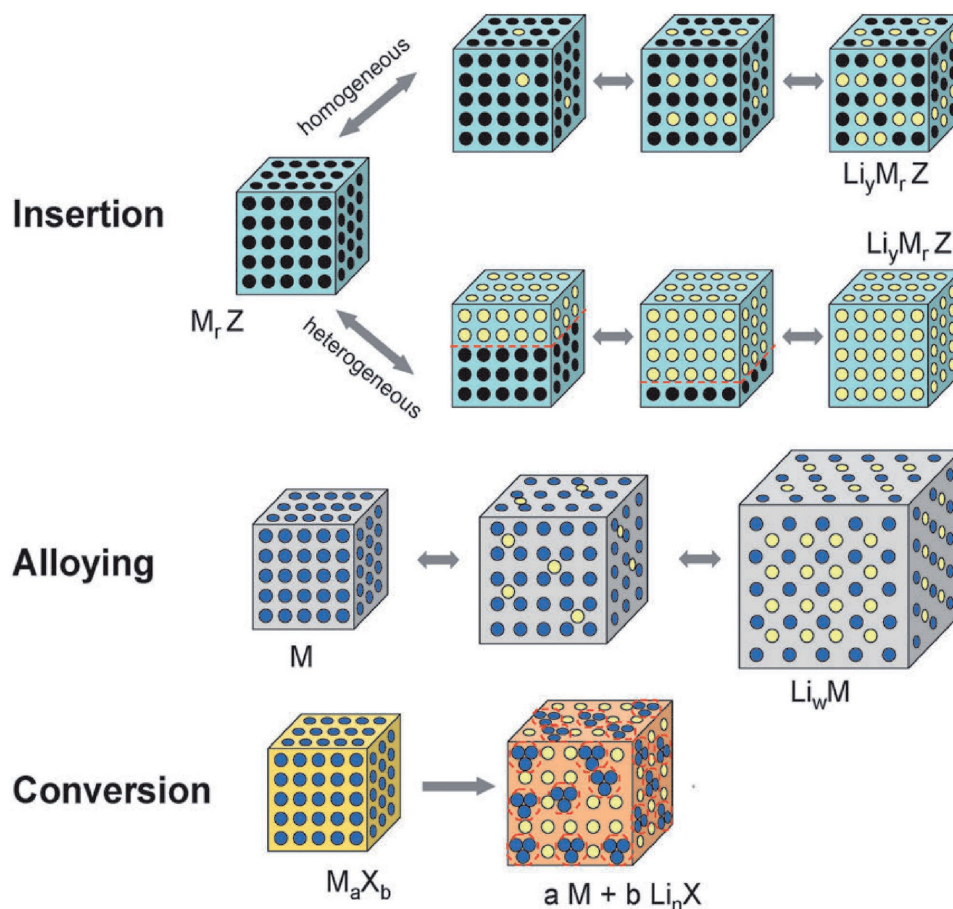


Figure 12. Schematic representation of the different reaction mechanisms of anode materials for LIBs. Reproduced with permission.^[118] Copyright 2009, The Royal Society of Chemistry.

into graphite crystallites, and then are stored in micropores.^[119] Mesopores not only provide Li^+ transport channels, but also improve the penetration of electrolyte. Thus, porous carbons have higher capacities than commercial graphite.^[120–122] Chen et al. used chemical vapor deposition (CVD) to prepare porous CNT networks on a carbon fibre paper, delivering a high reversible capacity of 546 mAh g^{-1} after 50 cycles at 0.05 mA cm^{-2} .^[121] Zhang and co-workers designed and synthesized N,S-codoped hierarchically porous graphene (DHPG) through an in situ construction strategy in Ni foam using graphene oxide (GO), sulfonated polystyrene (S-PS) spheres, and poly(vinyl pyrrolidone) (PVP) as the original materials.^[122] The DHPG delivered high rate capability (560 mAh g^{-1} at 5 A g^{-1} and 220 mAh g^{-1} at 80 A g^{-1}).

Spinel-type $\text{Li}_4\text{Ti}_5\text{O}_{12}$ can reversibly react with 3Li^+ to form $\text{Li}_7\text{Ti}_5\text{O}_{12}$ with a redox potential of $\approx 1.55 \text{ V}$, which avoids the formation of lithium dendrites when $\text{Li}_4\text{Ti}_5\text{O}_{12}$ is used as the anode in full cells.^[123–125] Furthermore, the structural change of $\text{Li}_4\text{Ti}_5\text{O}_{12}$ during the charge/discharge process is $\approx 0\%$, leading to durable cycling stability. $\text{Li}_4\text{Ti}_5\text{O}_{12}$ suffers, however, from its intrinsically low electrical conductivity ($10^{-13} \text{ S cm}^{-1}$) and Li^+ ion diffusion coefficient ($10^{-13} \text{ cm}^2 \text{ s}^{-1}$), resulting in poor rate performance. To solve these issues, two strategies have been proposed.^[126–129] One is to prepare nanoporous structures to achieve fast Li^+ ion transport. Feckl et al. prepared

highly porous $\text{Li}_4\text{Ti}_5\text{O}_{12}$ by the hydrothermal method combined with heat treatment.^[126] The $\text{Li}_4\text{Ti}_5\text{O}_{12}$ presented an ultrasmall crystal size of 3 nm and a uniform pore size of 7 nm . The mesoporous nanostructure enabled excellent high-rate capability (173 mAh g^{-1} at 100 C and 128 mAh g^{-1} at 800 C). The other strategy is surface modification by applying carbon materials or oxides.^[130,131] Our group investigated the effect of the thickness of carbon-coating on $\text{Li}_4\text{Ti}_5\text{O}_{12}$ on its electrochemical performance.^[130] For pristine $\text{Li}_4\text{Ti}_5\text{O}_{12}$, Li^+ ions could easily pass through the particle surface, but electron transport was limited (Figure 13a). A thin carbon layer ($\approx 2 \text{ nm}$) boosted both the electronic conduction along the carbon matrix and Li^+ transport through the defects and vacancies of carbon (Figure 13b). When the thickness of the carbon layer was more than 10 nm , the Li^+ diffusion distance became longer, and even Li^+ transport was hampered due to graphitic stacking (Figure 13c). Thus, it was necessary to balance the electronic and the ionic transport by adjusting the thickness of the carbon layer. So far as the low capacity of $\text{Li}_4\text{Ti}_5\text{O}_{12}$ is considered, the *p*-type semiconductor NiO_x was employed by Kang and co-workers to coat $\text{Li}_4\text{Ti}_5\text{O}_{12}$ to expand its working voltage range to reach high capacity,^[132] which was attributed to the ability of the coating to suppress the electrochemical reduction reactions of the organic solid electrolyte interphase (SEI) films and promote reversibility of the Li^+ transport process, as well as the rate capability

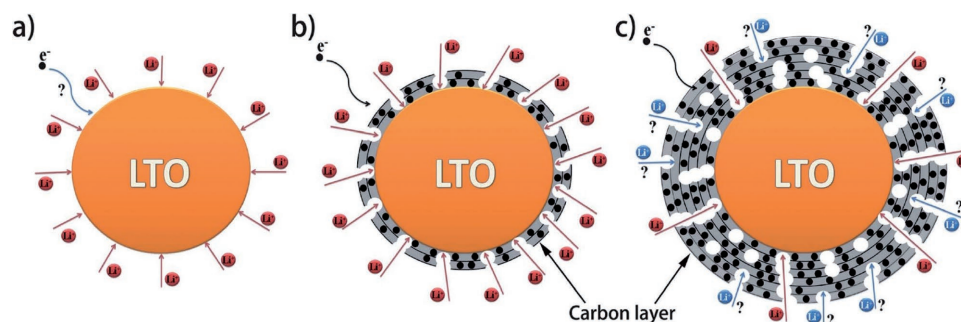


Figure 13. Schematic illustration of the electronic conductivity and Li^+ transport in a) bare LTO particles, b) LTO particles coated by a thin carbon layer, and c) LTO particles coated by a thick carbon layer with randomly distributed defects and vacancies. Reproduced with permission.^[130] Copyright 2013, The Royal Society of Chemistry.

and cyclability. Also, they attempted to synthesize hybrid nanocomposites combining $\text{Fe}/\text{Fe}_3\text{O}_4$ and $\text{Li}_4\text{Ti}_5\text{O}_{12}$ components as a coating.^[133] Desirable performance with high capacity and reversibility and stability was achieved, resulting from the conversion reaction of Fe_3O_4 , and the zero-strain feature and superb kinetics of $\text{Li}_4\text{Ti}_5\text{O}_{12}$.

Considering the Li^+ transport mechanism of insertion-type materials, porous structures are indispensable for storing Li^+ , providing Li^+ transport pathways, increasing the contact between the active materials and the electrolyte, and promoting the cyclability and rate capability of low-cost and environmentally friendly anodes. Notably, $\text{Li}_4\text{Ti}_5\text{O}_{12}$ as a zero-strain host material offers great promise for next-generation Li-ion batteries with high safety. Carbon-coated nanoporous $\text{Li}_4\text{Ti}_5\text{O}_{12}$ is a very attractive candidate for achieving high rate capability and long-term cyclability.

3.2. Alloying-Type Materials

Alloying-type materials converge on the IV and V groups, including Si, Ge, Sn, P, and Sb, which are receiving extensive interest. Each atom of alloying-type materials can theoretically accommodate 4.4 or 3 Li^+ , offering very high discharge capacities. The huge volume changes during alloying and dealloying processes, however, cause serious pulverization of the electrode materials and separation from the current collector, which severely restricts their practical application. A series of composites of alloying-type materials have been designed to solve this problem.

3.2.1. Si-Based Materials

Among the anode materials discussed so far, Si displays the highest theoretical specific capacity (4200 mAh g^{-1}), based on a $4.4 e^-$ alloying reaction with a redox potential of $\approx 0.4 \text{ V}$.^[134–136] Early in 2007, our group prepared nest-like Si nanospheres through a solvothermal route and investigated their superior lithium-storage capacity, demonstrating their potential application as anode materials for LIBs.^[137] Huge volume expansion ($\approx 400\%$), however, and semiconductor-level conductivity limit the cycling performance and rate capability of Si-based materials.^[138–141] What is more, the formation of SEI on the surface of Si nanoparticles (NPs) is unavoidable and related to the

electrolyte side reactions. The huge volume variation will inevitably rupture the SEI film and the excessive growth of SEI leads to battery failure. Different nanostructures of Si combined with electrically conductive carbon are commonly used to buffer the strain induced by volume change and enhance the conductivity.^[142–145] In this kind of alloy reaction-type material with large volume expansion, the yolk-shell structure is superior to the core-shell structure,^[146] as is well described in Figure 14. A conventional core-shell coating could not prevent repeated rupturing and reforming of the SEI on the surface of the electrode during cycling, but there is enough void space in the yolk-shell architecture to accommodate volume expansion volume, so as to make both the SEI layer on the surface of the electrode and the self-supporting framework stable. Cui and co-workers designed and prepared pomegranate-like yolk-shell Si@C composite by assembling Si@SiO₂@C clusters, and they delivered 97% capacity retention after 1000 cycles at 0.5 C.^[142] The assembled pomegranate-like micro/nanostructured spheres offered inner void space between each Si NP and the carbon coating layer to accommodate the volume expansion without rupturing the coating layer, which ensured the formation of a stable and thin SEI layer on the outer surface of the carbon. Cho and co-workers synthesized amorphous silicon nanoparticles anchored in 3D porous graphene by SiH₄ decomposition.^[143] The uniformly dispersed small Si nanoparticles (less than 10 nm) and the highly conductive graphene improved the kinetics of the reaction and electrode integration. The composite exhibited outstanding rate capability (2450 mAh g^{-1} at 2.8 A g^{-1} , 1622 mAh g^{-1} at 14 A g^{-1} , and 1148 mAh g^{-1} at 28 A g^{-1}) and long-term cycling stability (100% capacity retention after 1000 cycles at 14 A g^{-1}). In addition, other conductive materials are also formed into composites with Si to make up for the defects of pure Si. For example, Song et al. achieved Si/Ge double-layered nanotubes by employing a template-assisted synthesis method based on chemical vapor deposition.^[147] The heterostructured arrays exhibited stable capacity retention (85% after 50 cycles) and double the capacity at 3 C compared with the homogeneous Si system.

3.2.2. P-Based Materials

P is another promising anode, with the second highest theoretical specific capacity of 2595 mAh g^{-1} , based on the reaction

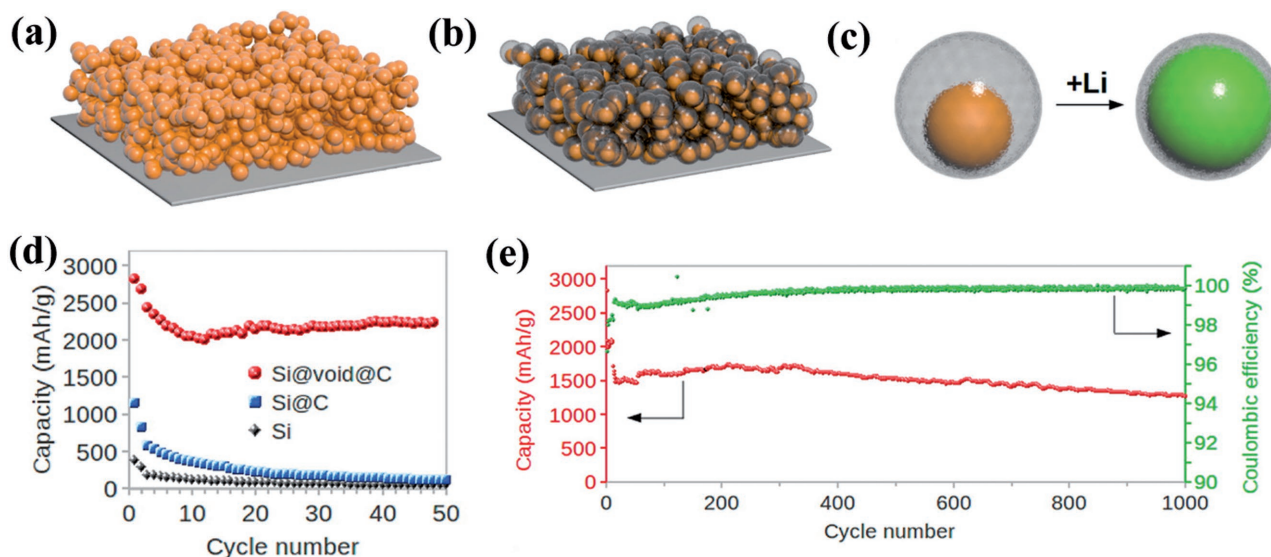


Figure 14. Schematic illustration of materials design for alloying reaction. a) A conventional slurry coated SiNP electrode. b) A novel Si@void@C electrode. c) A magnified schematic illustration of an individual Si@void@C particle. d) Galvanostatic cycling of different silicon nanostructures. e) Delithiation capacity and Coulombic efficiency (CE) of the first 1000 galvanostatic cycles for Si@void@C electrodes. Reproduced with permission.^[146] Copyright 2012, American Chemical Society.

of $3\text{Li} + \text{P} \leftrightarrow \text{Li}_3\text{P}$. Nevertheless, P suffers from the same problems as Si. So far, many reports on P anode feature the use of P–C composites to promote the performance.^[148–152] He's group fabricated P/C composite by heating red P and porous carbon at 450°C in a sealed vessel.^[148] The composite delivered a discharge capacity of 2413 mAh g^{-1} in the first cycle, with capacity retention of 87% from the second cycle to the 55th cycle at 0.1 A g^{-1} . Yang et al. reported a black phosphorus/graphite composite (Figure 15a) via a high-energy mechanical milling process.^[149] The layered black P and graphite were linked by P–C bonds, contributing to good structural stability. The composite displayed a high discharge capacity of 2786 mAh g^{-1} in the first cycle at 0.2 C with 80% capacity retention after 100 cycles (Figure 15b). Even at higher rates, high discharge capacities were obtained (1750 and 1240 mAh g^{-1} at 1 C and 4.5 C , respectively). Recently, a sublimation-induced strategy was adopted for the first time to synthesize 2D holey

phosphorus-based nanosheets, in which small nanoparticles tended to form.^[153] The phosphorus composite nanosheets yielded a high capacity of 630 mAh g^{-1} at high current density of 20 A g^{-1} , which was attributed to the helpful nature of the holey nanosheet structure for lithium-ion diffusion and electron transfer. Additionally, another way to overcome the volume expansion and poor conductivity is to prepare alloy compounds in the form of M_xP_y ($\text{M} = \text{Fe}, \text{Co}, \text{Ni}, \text{etc.}$). Wang and co-workers obtained core-shell structured $\text{Ni}_5\text{P}_4/\text{C}$ via a wet-chemistry reaction and a solid-state reaction.^[152] The carbon shell enhanced the conductivity of the composite, relieved the volume expansion, and suppressed the aggregation of the active particles, comprehensively keeping the structure stable and reversible during cycling. Even though P-based materials serve as one of the most prominent high-capacity anodes, mechanical milling is the general method to take advantage of their high capacity, and there have been few reports on real chemical methods.

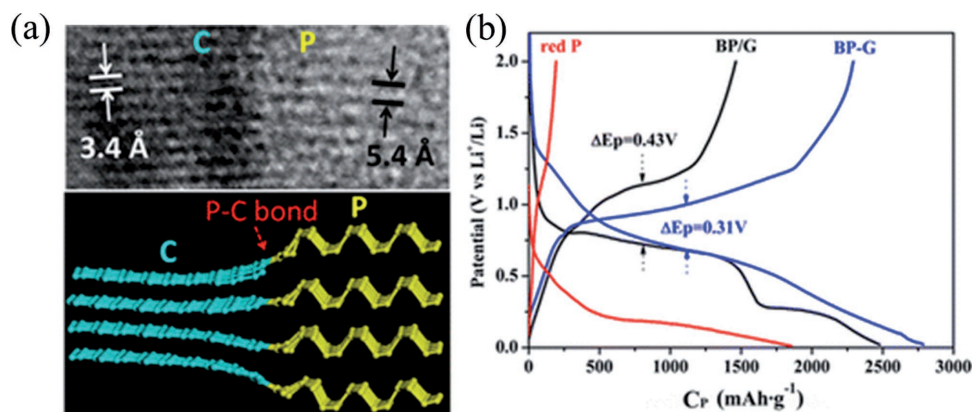


Figure 15. a) High-resolution TEM (HRTEM) image and schematic diagram of BP-G composite. b) The charge-discharge profiles of red P, BP/G, and BP-G electrodes at the first cycle between 0.01 and 2.0 V with a current density of 0.2 C . Reproduced with permission.^[149] Copyright 2014, American Chemical Society.

Therefore, building hierarchical structures for P-based electrodes through an effective chemical strategy, fully utilizing the intrinsic features of high capacity and low potential, is a novel perspective that can further promote the development of anode materials for LIBs.

3.2.3. Sn-Based Materials

Sn has also attracted wide interest because of its high theoretical specific capacity (992 mAh g^{-1}) based on a $4.4 e^-$ alloying reaction.^[12] Due to the large volume expansion, Sn-based composites have been proposed to maintain the structural integrity.^[154–156] Scrosati and co-workers reported nanostructured Sn–C composites as negative electrode for LIBs.^[157,158] These Sn–C composites were prepared by gel carbonization after the infiltration of tin precursor into an organic gel, and it was proved that a calcination step with the volume contraction is favorable for the reversible Li^+ insertion/deinsertion process.^[157] Then, they implemented the optimized scheme to improve the electrochemical performance of Sn–C composite.^[158] Our group also prepared two kinds of Sn nanoparticles embedded in carbon matrix. The ultrasmall Sn nanoparticles ($\approx 5 \text{ nm}$) homogeneously embedded in N-doped porous carbon were fabricated by carbonizing the Sn(Salen) (Figure 16a,b).^[23] The Sn/C composite showed high discharge capacities of 1014 mAh g^{-1} at 0.2 A g^{-1} and 480 mAh g^{-1} at 5 A g^{-1} . The excellent rate performance is attributed to the combination of the small particle size of Sn and the good conductive network of porous carbon. Furthermore, Our group used an aerosol spray pyrolysis to synthesize pitaya-like Sn@C nanocomposite, in which small Sn nanoparticles ($\approx 8 \text{ nm}$) were uniformly dispersed in the spherical carbon matrix (Figure 16c,d).^[159] The nanocomposite exhibited an initial discharge capacity of $1007.1 \text{ mAh g}^{-1}$ and maintained a

reversible capacity of 910 mAh g^{-1} after 180 cycles at 0.2 A g^{-1} . Even at 16 A g^{-1} , the discharge capacity reached 205.3 mAh g^{-1} . Qin et al. fabricated 3D porous graphene networks anchored with Sn@graphene through an in situ chemical vapor deposition technique,^[160] in which the metal served as a catalyst and self-assembled NaCl particles served as template. The results showed that the 3D hybrid anode possessed a high capacity of 682 mAh g^{-1} even at 2 A g^{-1} and capacity retention of $\approx 96.3\%$ after 1000 cycles, along with a very high rate performance ($1022, 865, 780, 652, 459,$ and 270 mAh g^{-1} at $0.2, 0.5, 1, 2, 5,$ and 10 A g^{-1} , respectively). In addition, Sn-based materials, including SnO_2 and SnS_2 , have stimulated much research due to the appearance of a high-capacity alloy reaction following the conversion reaction during the first cycle.^[161,162] Guo and co-workers proposed an in situ hydrazine monohydrate vapor reduction method to achieve SnO_2 nanocrystals in graphene sheets ($\text{SnO}_2 \text{ NC@N-RGO}$),^[127] which displayed a high capacity of 1352 mAh g^{-1} . Furthermore, Mai and co-workers synthesized heterogeneous branched core–shell SnO_2 –polyaniline (PANI) nanorod arrays through electrodeposition and SnO_2 quantum dots@graphene oxide with good dispersion through an in situ reduction process.^[163,164] Both forms of SnO_2 yielded significant improvements in rate performance as well as in cycling stability for LIBs. SnS_2 , with a layered CdI_2 -type structure, was incorporated into 2D graphene– SnS_2 hybrids with a novel porous nanoarchitecture for the first time.^[165] This structure effectively alleviated the large volume expansion and controlled the capacity fading, delivering high reversible capacity ($\approx 650 \text{ mAh g}^{-1}$) and excellent high-rate capability ($\approx 230 \text{ mAh g}^{-1}$ at 6400 mA g^{-1}).

3.2.4. Ge-Based Materials

Ge is another common alloy reaction-type materials. Similar to the above, Ge also suffers from serious volume expansion during the charge/discharge process. Usually, the electrical conductivity of Ge is 10 000 times greater than that of Si, and the ion diffusivity of Ge is about 400 times higher than that of Si.^[166] Therefore, many chemists have devoted themselves to the design and modification of the morphology and structure of Ge. Lu and co-workers prepared core–shell Ge@graphene@ TiO_2 nanofibers through electrospinning followed by atomic layer deposition, and they exhibited outstanding electrochemical performance in LIBs.^[167] The capacity of the composite could be maintained at 1050 mAh g^{-1} after 100th cycle at a current density of 100 mA g^{-1} . Such an excellent performance stems from the design of the core–shell structure. Specifically, graphene-doped nanofibers acted as an electrolyte blocking layer to prevent the formation of SEI and functioned as the mechanical backbone, as well as a conductive medium, while the outer shell of TiO_2 ensures the structural integrity. In addition, graphene and TiO_2 can both protect germanium nanofibers from the volume expansion in the charge/discharge process. 3D porous germanium–carbon composite was prepared by Park and co-workers^[168] and it showed excellent cyclability and rate performance (charge capacity of 1216 mAh g^{-1} , even after 1000 cycles at a 2 C rate, and an average capacity of 429 mAh g^{-1} , even at an ultrahigh charge rate of 400 C

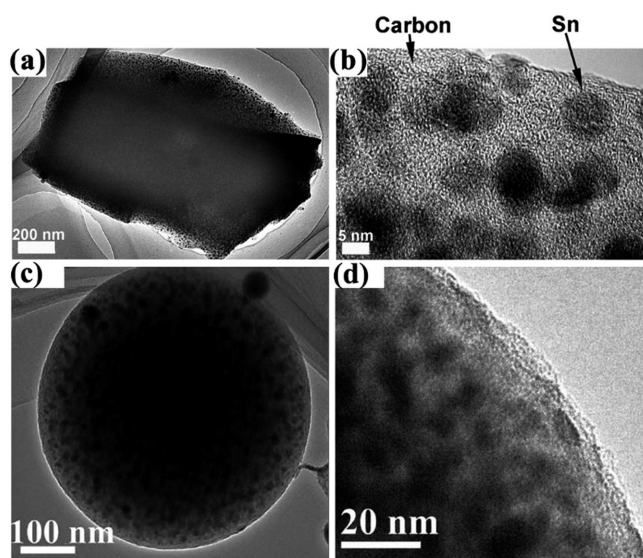


Figure 16. TEM and HRTEM images of ultrasmall Sn nanoparticles dispersed in a,b) N-doped porous carbon matrix and c,d) pitaya-like Sn@C nanocomposite. Reproduced with permission.^[23,159] Copyright 2013, American Chemical Society and Copyright 2014, The Royal Society of Chemistry.

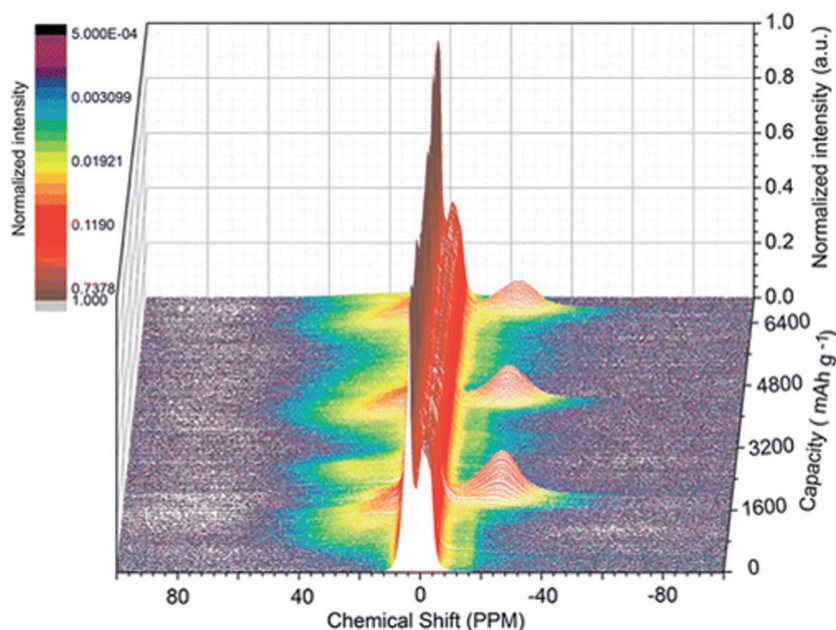


Figure 17. ^7Li NMR spectra of Ge@CNT color-mapped in situ during lithiation and delithiation cycles. Reproduced with permission.^[169] Copyright 2015, American Chemical Society.

(640 A g⁻¹). Importantly, Ge nanorods encapsulated by bamboo-type multiwalled carbon nanotubes (Ge@CNT) were fabricated via the use of Ge nanoparticles as seeds and an in situ investigation on the effectiveness of the core-shell design was conducted.^[169] The in situ ^7Li NMR (Figure 17) and TEM results revealed that the unique capsule-like configuration protects Ge@CNT against volume changes and that amorphous and crystalline phases both exist during Li alloying and dealloying processes, shining light on the origin of the reversibility and high capacity. This research helps us understand how the core-shell design protects the structural stability, especially for alloy reaction-type anode materials.

Alloys, such as Sn-Sb, Sn-P, and Ge-P, are also a promising group of high-capacity anode materials, offering their respective advantages including high capacity, highly ductile phase, and electronic conductivity. Similarly, various strategies, such as carbon coating and silica shell coating, were employed to address the problems of volume change and pulverization that exist in alloy materials.^[170] Nanoparticles of SnSb alloy coated on the surface of multiwalled carbon nanotubes result in obvious improvement in electrochemical performance, stemming from the decrease in the dramatic volume variation and agglomeration of SnSb alloys.^[170] Zhou and co-workers synthesized the layer-structured metal phosphide GeP₅ as anode material for LIBs for the first time by simple mechanical milling.^[171] GeP₅ as anode material exhibits a large specific capacity of 2266 mAh g⁻¹ for Li storage, which is attributed to the reactive elements Ge and P. Next, by forming a composite with conductive carbon, the electrochemical performance of GeP₅ was notably improved, originating from the homogeneous distribution of the active GeP₅ and the good buffering mechanism provided by the carbon matrix. Recently, Ge@Si core-shell nanostructures were formed in a controllable way, based on minimization of the total Gibbs free energy and the nanoscale Kirkendall effect.^[172] They

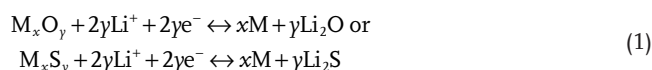
delivered a reversible capacity of 590 mAh g⁻¹ after 100 cycles at 200 mA g⁻¹ between 0.01 and 1.5 V, and rate capacity of 916, 779, and 666 mAh g⁻¹ at 200, 500, and 1000 mA g⁻¹, respectively, which is attributed to the unique hollow structure for effectively alleviating structural stress during repeated Li⁺ insertion/extraction processes.

Although alloy-reaction-type anode materials have large specific capacity, they commonly suffer from huge volume changes, which cause the capacity to fade in a linear way during Li⁺ intercalation/deintercalation processes. Much effort has been devoted to the rational design of hierarchical structures to overcome these issues. The advantage of embedded nanostructured Si/C, P/C, Sn/C, and Ge/C composites, delivering enhanced cycling and rate performance, are related to the enhancement of conductivity and the stability of the pristine architecture, alleviating the problems of pulverization and abscission. The core/yolk-shell and porous structures, on the one hand, can provide sufficient space to accommodate the severe volume expansion during discharge. On the other hand, the shell and pores are self-supporting frameworks that are conducive to stabilizing the SEI film and fixing the active sample in an interior space. Considering the high-capacity of the alloying-type anode materials, we should focus on the complementary advantages of some elements and the effective self-assembly of micro/nano-perfect structures, as well as scalable preparation strategies.

On the other hand, the shell and pores are self-supporting frameworks that are conducive to stabilizing the SEI film and fixing the active sample in an interior space. Considering the high-capacity of the alloying-type anode materials, we should focus on the complementary advantages of some elements and the effective self-assembly of micro/nano-perfect structures, as well as scalable preparation strategies.

3.3. Conversion-Type Materials

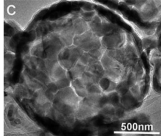
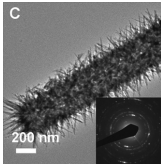
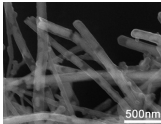
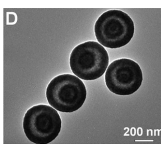
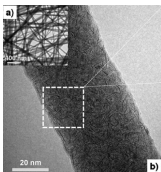
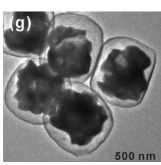
Some metal oxides and sulfides can react with Li⁺ via a conversion reaction as follows^[173–180]



(M = Fe, Co, Ni, Cu, Mn, etc.)

Though the theoretical specific capacity is high, the large structural changes limit their cyclability. In addition, metallic M is easily separated from Li₂O (or Li₂S), leading to the loss of active materials. Most oxides and sulfides are semiconductors, and their electronic conductivities are not high enough, which limits their rate capability. A series of core-shell structured, multishell hollow structured, and micro/nano-hierarchically structured oxides, sulfides, and their carbon-based composites are used to solve these problems.^[178,181–187] Table 2 summarizes the morphology and electrochemical performance of some representative oxides and sulfides. These hierarchically structured oxides and sulfides have achieved improved rate and cycling performance. For example, Zhang et al. employed a microemulsion-mediated process to prepare cog-shaped CuO nanoparticles assembled on Cu electrodes.^[188] The hierarchical nanofilament-based structures shortened the

Table 2. Various hierarchical structure and electrochemical performance of some representative oxides and sulfides. Images are: Reproduced with permission.^[194] Copyright 2015, Royal Society of Chemistry. Reproduced with permission.^[181] Copyright 2014, Wiley-VCH. Reproduced with permission.^[195] Copyright 2013, Wiley-VCH. Reproduced with permission.^[196] Copyright 2014, American Chemical Society. Reproduced with permission.^[197] Copyright 2015, Wiley-VCH. Reproduced with permission.^[182] Copyright 2014, Wiley-VCH. Reproduced with permission.^[199] Copyright 2015, Wiley-VCH. Reproduced with permission.^[200] Copyright 2016, Wiley-VCH.

Oxides and sulfides	Morphology	Rate performance	Cycling performance	Refs.
Porous multideck-cage structured Fe ₃ O ₄ @C		850 mAh g ⁻¹ at 1 A g ⁻¹	1100 mAh g ⁻¹ after 50 cycles at 0.2 A g ⁻¹	[194]
Hierarchically tubular structured Fe ₂ O ₃ @C		962 mAh g ⁻¹ at 0.8 A g ⁻¹	1126 mAh g ⁻¹ after 70 cycles at 0.2 A g ⁻¹ (≈98% capacity retention)	[181]
Triple-shelled Co ₃ O ₄ hollow spheres		1117.3 mAh g ⁻¹ at 2 A g ⁻¹	1615.8 mAh g ⁻¹ after 30 cycles at 0.05 A g ⁻¹ (100.16% capacity retention)	[195]
Peapod-like MnO/C composite		1119 mAh g ⁻¹ at 0.5 A g ⁻¹ and 463 mAh g ⁻¹ at 5 A g ⁻¹	525 mAh g ⁻¹ after 1000 cycles at 2 A g ⁻¹	[196]
Double-shell NiCo ₂ O ₄ hollow spheres		834, 745, 662, and 533 mAh g ⁻¹ at 0.3, 0.6, 1, and 2 A g ⁻¹ , respectively	706 mAh g ⁻¹ after 100 cycles at 0.2 A g ⁻¹ (78% capacity retention)	[197]
Single-layered ultrasmall MoS ₂ nanoplates embedded in carbon nanofibers		1095, 986, 768, 548, and 374 mAh g ⁻¹ at 0.5, 1, 5, 10, and 50 A g ⁻¹ , respectively	1007 mAh g ⁻¹ after 100 cycles at 1 A g ⁻¹ and 661 mAh g ⁻¹ after 1000 cycles at 10 A g ⁻¹	[198]
Uniform Fe ₃ O ₄ hollow spheres		992, 853, 716, 548, and 457 mAh g ⁻¹ at 1, 2, 4, 8, and 10 A g ⁻¹ , respectively	700 mAh g ⁻¹ at 3 A g ⁻¹ without notable fading over 200 cycles	[199]
Yolk-shelled Fe ₃ O ₄ @carbon		1012, 890, 800, 695, 575, 477, and 370 mAh g ⁻¹ at 0.1, 0.5, 1, 2, 5, 10, and 20 C, respectively	900 mAh g ⁻¹ after 2000 cycles at 5 C, 470 mAh g ⁻¹ after 8000 cycles	[200]

lithium ion diffusion paths, and the mesoscale assembly of the CuO nanostructures provided enough room to accommodate swing stress during lithium insertion and removal. At the same time, the distance between CuO microparticles in arrays offers a large electrode/electrolyte contact area and decreases

the polarization of the electrode during the discharge/charge cycling, thereby enhancing the electrode's electrochemical performance in lithium-ion batteries. Wang and co-workers prepared three kinds of microspheres via a template method, that is, multishell α -Fe₂O₃ hollow microspheres, Co₃O₄ hollow

sphere, and multishelled TiO₂ hollow microspheres.^[189] Taking multishelled α -Fe₂O₃ hollow microspheres for example, thin triple-shelled α -Fe₂O₃ spheres showed better performance than those of single-, double-, and quadruple-shelled ones because of their suitable volume occupation rate and stable shell. The triple-shelled α -Fe₂O₃ microspheres delivered a high capacity of 1702 mAh g⁻¹ at 0.05 A g⁻¹, which originated from not only the active material Fe₂O₃, but also the interior cavities for Li⁺ storage. Another two types of microspheres presented the same principle as the Fe₂O₃ materials. Lou and co-workers synthesized needle-like Co₃O₄ nanotubes, employing a one-step self-supported topotactic transformation approach, as electrode materials for lithium ion batteries.^[190] In addition, Mai and co-workers prepared an amorphous vanadium oxide matrix supporting hierarchical porous Fe₃O₄/graphene nanowires by a template-free hydrothermal method and subsequent heat treatment.^[191] This hierarchical anode manifested high capacity (1146 mAh g⁻¹), fantastic rate capability (5 A g⁻¹), and very good cycling stability, which is related to the unique porous hybrid nanowire architecture. Metal organic frameworks (MOFs), a novel class of porous materials, have attracted great interest when considered as precursors for hierarchical structures. Cho's group rationally took advantage of MOFs to obtain spindle-like mesoporous α -Fe₂O₃ as anode material for high-rate lithium ion batteries. Recently, Lou and co-workers continuously designed a different strategy for the synthesis of novel hierarchical tubular structures composed of Co₃O₄ hollow nanoparticles and carbon nanotubes (**Figure 18**) produced using sacrificial zeolitic imidazolate framework-67 (ZIF-67) through a two-step annealing treatment.^[192] The as-prepared hierarchical hybrid showed excellent cycling and rate performance, delivering capacity of 782 and 577 mAh g⁻¹ after 200 cycles at 1 and 4 A g⁻¹, respectively. Yu and co-workers synthesized ultra-small single-layered MoS₂ nanoplates embedded in carbon nanofibers by electrospinning.^[182] The MoS₂/C composite displayed high capacities of 1095, 768, 548, and 374 mAh g⁻¹ at 0.5, 5, 10, and

50 A g⁻¹, respectively. The single-layered MoS₂ provided high capacity based on interfacial Li⁺ storage, Li⁺ intercalation (MoS₂ + x Li⁺ + x e⁻ \leftrightarrow Li _{x} MoS₂), and phase conversion (Li _{x} MoS₂ + (4- x)Li⁺ + (4- x)e⁻ \leftrightarrow Mo + 2Li₂S). Meanwhile, the carbon fibers not only improved the electronic conductivity but also provided a nanoconfinement effect. Subsequently, Yu and co-workers systematically explored a facile approach resulting in 0D transition-metal sulfide nanoparticles embedded in 1D porous carbon nanowires embedded in a 3D graphene network (NiS, CoS, and MnS).^[193] This structure is complex and possesses the properties of a multiscale, multidimensional, and hierarchically ordered structure, which is helpful for the immersion in electrolyte, the diffusion of Li⁺ ions and electrons, and the maintenance of the structure. All these advantages will optimize the reversibility, cycling stability, and rate capability of the anode, holding great promise for future lithium energy storage.

Although conversion-type materials with hierarchical structure deliver high capacity, even more than the theoretical value, due to the surface adsorption and pore/defect storage, \approx 50% charge capacity of conversion-type materials is obtained in the voltage range of 1.5–3.0 V. Therefore, the conversion-type materials only couple with cathode materials with high potential.

In this section, many anode materials have been reviewed. The anode materials relying on insertion reaction exhibit relatively low theoretical specific capacity. Commercial graphite works in a low potential for Li⁺ insertion, accompanied by the formation of lithium dendrites, the dissolution of electrolyte, and certain safety problems. Spinel-type Li₄Ti₅O₁₂ possesses high safety, which is expected for use in scalable energy storage. Carbon-coating combined with a porous structure can effectively improve the electronic and ionic transport. Alloying-type materials, such as Si, Sn, P, and Ge, show high reversible capacity, but suffer from huge volume changes. Ultrafine nanoparticles embedded in highly conductive carbon matrix and core/yolk-shell porous structures can enhance the cycling and rate performance. Conversion-type materials also

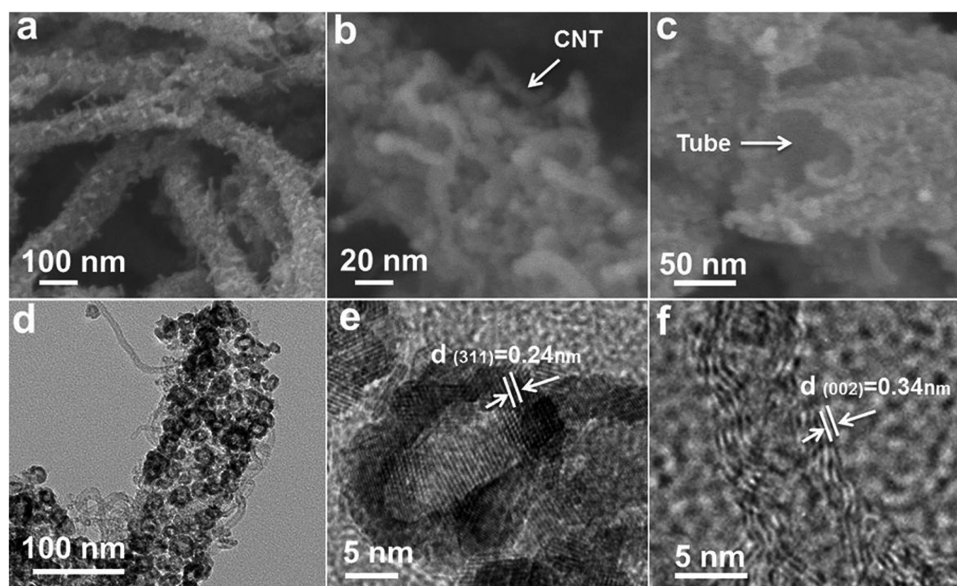


Figure 18. a–c) FESEM, d) TEM, and e,f)HRTEM images of the synthesized hierarchical CNT/Co₃O₄ microtubes. Reproduced with permission.^[192] Copyright 2016, The Royal Society of Chemistry.

Received: May 23, 2017

Revised: July 5, 2017

Published online:

possess high theoretical specific capacity, but they face the challenges of large structural and volume changes. Multishell hollow structures and carbon-coating are common strategies to enhance structural stability and Li⁺ diffusion. Combinations of high-capacity anode and cathode materials are clearly needed in further studies to increase the capacity of LIBs.

4. Conclusion

The relationship between material structure and performance is a perpetual truth. For cathode materials, microstructures assembled from nanoparticles (i.e., LiNi_{1/3}Mn_{1/3}Co_{1/3}O₂), combined with surface modification offer improved structural stability and rate performance. Core-shell or concentration-gradient architectures (i.e., Ni-rich LiNi_{1-x-y}Co_xMn_zO₂) exhibit high capacity (over 200 mAh g⁻¹) with high capacity retention. 1D porous Mn-based spinels assembled from nanoparticles promote reaction kinetics and electrode integration. Nanocomposites of lithiated transition-metal phosphates/silicates and carbon materials feature enhanced conductivity and cycling stability. In terms of anode materials, Si/C, Sn/C, and Ge/C composites with embedded structures, porous Li₄Ti₅O₁₂/C composites, and multishell hollow metal oxides all have achieved high rate and cycling performances. Besides, coating layer of organic electrode materials has also been explored to confine the active samples for achieving desirable capacity and promoted cycling stability.

Although the materials with hierarchical structure have realized great progress, there are still some challenges. Novel preparation routes with fewer steps and lower cost should be developed to realize commercialization. Actually, each material has its own strengths and deficiencies. Combining the merits of compatible materials plus the rational design of architectures is an effective way to enhance the electrochemical performance of cathode and anode materials for LIBs. In addition, in situ observation of changes in hierarchical structures during Li⁺ intercalation/deintercalation is expected to be reported. In order to achieve large-scale production and deeply reveal the interaction mechanisms, more studies should focus on reasonable designs and in-situ characterization of hierarchical structures in the future.

Acknowledgements

This work was supported by the National Key R&D Program of China (2016YFB0901502), and the National Natural Science Foundation of China (Nos.51271094, 51371100). K.Z. acknowledges Korea Research Fellowship Program through the National Research Foundation of Korea (NRF) funded by the Ministry of Science, ICT and Future Planning (No. 2016H1D3A1906790).

Conflict of Interest

The authors declare no conflict of interest.

Keywords

cathode and anode materials, hierarchical structures, high performance, lithium-ion batteries

- [1] B. Dunn, H. Kamath, J.-M. Tarascon, *Science* **2011**, *334*, 928.
- [2] M. S. Whittingham, *Chem. Rev.* **2014**, *114*, 11414.
- [3] K. Zhang, X. Han, Z. Hu, X. Zhang, Z. Tao, J. Chen, *Chem. Soc. Rev.* **2015**, *44*, 699.
- [4] V. Etacheri, R. Marom, R. Elazari, G. Salitra, D. Aurbach, *Energy Environ. Sci.* **2011**, *4*, 3243.
- [5] N.-S. Choi, Z. Chen, S. A. Freunberger, X. Ji, Y.-K. Sun, K. Amine, G. Yushin, L. F. Nazar, J. Cho, P. G. Bruce, *Angew. Chem., Int. Ed.* **2012**, *51*, 9994.
- [6] F. Cheng, J. Liang, Z. Tao, J. Chen, *Adv. Mater.* **2011**, *23*, 1695.
- [7] O. K. Park, Y. Cho, S. Lee, H.-C. Yoo, H.-K. Song, J. Cho, *Energy Environ. Sci.* **2011**, *4*, 1621.
- [8] Z. Yang, J. Liu, S. Baskaran, C. Imhoff, J. Holladay, *JOM* **2010**, *62*, 14.
- [9] K. M. Abraham, *J. Phys. Chem. Lett.* **2015**, *6*, 830.
- [10] S. Peng, L. Li, Y. Hu, M. Srinivasan, F. Cheng, J. Chen, S. Ramakrishna, *ACS Nano* **2015**, *9*, 1945.
- [11] V. Aravindan, Y.-S. Lee, S. Madhavi, *Adv. Energy Mater.* **2015**, *5*, 1402225.
- [12] M. N. Obrovac, V. L. Chevrier, *Chem. Rev.* **2014**, *114*, 11444.
- [13] M. V. Reddy, G. V. Subba Rao, B. V. R. Chowdari, *Chem. Rev.* **2013**, *113*, 5364.
- [14] C. Masquelier, L. Croguennec, *Chem. Rev.* **2013**, *113*, 6552.
- [15] P. He, H. Yu, D. Li, H. Zhou, *J. Mater. Chem.* **2012**, *22*, 3680.
- [16] A. Kraysberg, Y. Ein-Eli, *Adv. Energy Mater.* **2012**, *2*, 922.
- [17] Z. Gong, Y. Yang, *Energy Environ. Sci.* **2011**, *4*, 3223.
- [18] K. Zhang, Z. Hu, Z. Tao, J. Chen, *Sci. China Mater.* **2014**, *57*, 42.
- [19] Y.-G. Guo, J.-S. Hu, L.-J. Wan, *Adv. Mater.* **2008**, *20*, 2878.
- [20] L. Su, Y. Jing, Z. Zhou, *Nanoscale* **2011**, *3*, 3967.
- [21] J. Xiao, J. Zheng, X. Li, Y. Shao, J. Zhang, *Nanotechnology* **2013**, *24*, 424004.
- [22] J. Li, C. Cao, X. Xu, Y. Zhu, R. Yao, *J. Mater. Chem. A* **2013**, *1*, 11848.
- [23] Z. Zhu, S. Wang, J. Du, Q. Jin, T. Zhang, F. Cheng, J. Chen, *Nano Lett.* **2013**, *14*, 153.
- [24] Y.-K. Sun, S.-T. Myung, M.-H. Kim, J. Prakash, K. Amine, *J. Am. Chem. Soc.* **2005**, *127*, 13411.
- [25] K. Zhang, Z. Hu, J. Chen, *J. Mater. Chem.* **2013**, *22*, 214.
- [26] W. Liu, P. Oh, X. Liu, M.-J. Lee, W. Cho, S. Chae, Y. Kim, J. Cho, *Angew. Chem., Int. Ed.* **2015**, *54*, 4440.
- [27] K. Mizushima, P. C. Jones, P. J. Wiseman, J. B. Goodenough, *Mater. Res. Bull.* **1980**, *15*, 783.
- [28] D. Cauranta, N. Baffie, B. Garcia, J. P. Pereira-Ramos, *Solid State Ionics* **1996**, *91*, 45.
- [29] S. M. Lee, S. H. Oh, W. I. Cho, H. Jang, *Electrochim. Acta* **2006**, *52*, 1507.
- [30] J. Lu, Q. Peng, W. Wang, C. Nan, L. Li, Y. Li, *J. Am. Chem. Soc.* **2013**, *135*, 1649.
- [31] Y.-K. Sun, S.-T. Myung, B.-C. Park, J. Prakash, I. Belharouak, K. Amine, *Nat. Mater.* **2009**, *8*, 320.
- [32] Y. K. Sun, Z. Chen, H. J. Noh, D. J. Lee, H. G. Jung, Y. Ren, S. Wang, C. S. Yoon, S. T. Myung, K. Amine, *Nat. Mater.* **2012**, *11*, 942.
- [33] Y. Kim, D. Kim, *ACS Appl. Mater. Interfaces* **2012**, *4*, 586.
- [34] M. Jo, M. Noh, P. Oh, Y. Kim, J. Cho, *Adv. Energy Mater.* **2014**, *4*, 1301583.
- [35] H. Yang, P. Liu, Q. Chen, X. Liu, Y. Lu, S. Xie, L. Ni, X. Wu, M. Peng, Y. Chen, Y. Tang, Y. Chen, *RSC Adv.* **2014**, *4*, 35522.

- [36] H. J. Meng, P. F. Zhou, Z. Zhang, Z. L. Tao, J. Chen, *Ceram. Int.* **2017**, *43*, 3885.
- [37] J.-H. Ju, K.-S. Ryu, *J. Alloys Compd.* **2011**, *509*, 7985.
- [38] P. F. Zhou, Z. Zhang, H. J. Meng, Y. Y. Lu, J. Cao, F. Y. Cheng, Z. L. Tao, J. Chen, *Nanoscale* **2016**, *8*, 19263.
- [39] Z. Zhang, P. F. Zhou, H. J. Meng, C. C. Chen, Z. L. Tao, J. Chen, *J. Energy Chem.* **2017**, *26*, 481.
- [40] Y. Koyama, Y. Makimura, I. Tanaka, H. Adachi, T. Ohzuku, *J. Electrochem. Soc.* **2004**, *151*, A1499.
- [41] R. Berthelot, D. Carlier, C. Delmas, *Nat. Mater.* **2011**, *10*, 74.
- [42] T. Ohzuku, Y. Makimura, *Chem. Lett.* **2001**, *30*, 642.
- [43] Q. Sa, E. Gratz, M. He, W. Lu, D. Apelian, Y. Wang, *J. Power Sources* **2015**, *282*, 140.
- [44] W.-H. Ryu, S.-J. Lim, W.-K. Kim, H. Kwon, *J. Power Sources* **2014**, *257*, 186.
- [45] Y. Huang, J. Chen, J. Ni, H. Zhou, X. Zhang, *J. Power Sources* **2009**, *188*, 538.
- [46] H.-S. Kim, Y. Kim, S.-I. Kim, S. W. Martin, *J. Power Sources* **2006**, *161*, 623.
- [47] P. R. Ilango, T. Subburaj, K. Prasanna, Y. N. Jo, C. W. Lee, *Mater. Chem. Phys.* **2015**, *158*, 45.
- [48] H. Yu, H. Zhou, *J. Phys. Chem. Lett.* **2013**, *4*, 1268.
- [49] Y. Jiang, Z. Yang, W. Luo, X. Hu, Y. Huang, *Phys. Chem. Chem. Phys.* **2013**, *15*, 2954.
- [50] J. Yang, F. Cheng, X. Zhang, H. Gao, Z. Tao, J. Chen, *J. Mater. Chem. A* **2014**, *2*, 1636.
- [51] J. Liu, A. Manthiram, *J. Mater. Chem.* **2010**, *20*, 3961.
- [52] M. Hou, S. Guo, J. Liu, J. Yang, Y. Wang, C. Wang, Y. Xia, *J. Power Sources* **2015**, *287*, 370.
- [53] J. Liu, L. Chen, M. Hou, F. Wang, R. Che, Y. Xia, *J. Mater. Chem.* **2012**, *22*, 25380.
- [54] M. N. Ates, S. Mukerjee, K. M. Abraham, *J. Electrochem. Soc.* **2015**, *162*, A1236.
- [55] M. N. Ates, S. Mukerjee, K. M. Abraham, *J. Electrochem. Soc.* **2014**, *161*, A355.
- [56] P. Oh, S.-M. Oh, W. Li, S. Myeong, J. Cho, A. Manthiram, *Adv. Sci.* **2016**, *3*, 1600184.
- [57] M. M. Thackeray, P. J. Johnson, L. A. de Picciotto, P. G. Bruce, J. B. Goodenough, *Mater. Res. Bull.* **1984**, *19*, 179.
- [58] J. M. Tarascon, E. Wang, F. K. Shokoohi, W. R. McKinnon, S. Colson, *J. Electrochem. Soc.* **1991**, *138*, 2859.
- [59] M. Yonemura, A. Yamada, H. Kobayashi, M. Tabuchi, T. Kamiyama, Y. Kawamoto, R. Kanno, *J. Mater. Chem.* **2004**, *14*, 1948.
- [60] Z.-J. Zhang, S.-L. Chou, Q.-F. Gu, H.-K. Liu, H.-J. Li, K. Ozawa, J.-Z. Wang, *ACS Appl. Mater. Interfaces* **2014**, *6*, 22155.
- [61] M. J. Lee, S. Lee, P. Oh, Y. Kim, J. Cho, *Nano Lett.* **2014**, *14*, 993.
- [62] J. Lu, C. Zhan, T. Wu, J. Wen, Y. Lei, A. J. Kropf, H. Wu, D. J. Miller, J. W. Elam, Y.-K. Sun, X. Qiu, K. Amine, *Nat. Commun.* **2014**, *5*, 5693.
- [63] F. Cheng, H. Wang, Z. Zhu, Y. Wang, T. Zhang, Z. Tao, J. Chen, *Energy Environ. Sci.* **2011**, *4*, 3668.
- [64] S.-M. Bak, K.-W. Nam, C.-W. Lee, K.-H. Kim, H.-C. Jung, X.-Q. Yang, K.-B. Kim, *J. Mater. Chem.* **2011**, *21*, 17309.
- [65] X. Xiao, J. Lu, Y. Li, *Nano Res.* **2010**, *3*, 733.
- [66] J. Luo, Y. Wang, H. Xiong, Y. Xia, *Chem. Mater.* **2007**, *19*, 4791.
- [67] M. R. Jo, Y.-I. Kim, Y. Kim, J. S. Chae, K. C. Roh, W.-S. Yoon, Y.-M. Kang, *ChemSusChem* **2014**, *7*, 2248.
- [68] J. Yang, X. Han, X. Zhang, F. Cheng, J. Chen, *Nano Res.* **2013**, *6*, 679.
- [69] L. Zhou, D. Zhao, X. Lou, *Angew. Chem., Int. Ed.* **2012**, *51*, 239.
- [70] S.-T. Myung, K.-S. Lee, D.-W. Kim, B. Scrosati, Y.-K. Sun, *Energy Environ. Sci.* **2011**, *4*, 935.
- [71] X. Zhang, F. Cheng, J. Yang, J. Chen, *Nano Lett.* **2013**, *13*, 2822.
- [72] X. Zhang, F. Cheng, K. Zhang, Y. Liang, S. Yang, J. Liang, J. Chen, *RSC Adv.* **2012**, *2*, 5669.
- [73] J. Yang, X. Zhang, X. Han, F. Cheng, Z. Tao, J. Chen, *J. Mater. Chem. A* **2013**, *1*, 13742.
- [74] A. K. Padhi, K. S. Nanjundaswamy, J. B. Goodenough, *J. Electrochem. Soc.* **1997**, *144*, 1188.
- [75] S.-Y. Chung, J. T. Bloking, Y.-M. Chiang, *Nat. Mater.* **2002**, *1*, 123.
- [76] H. Liu, F. C. Strobridge, O. J. Borkiewicz, K. M. Wiaderek, K. W. Chapman, P. J. Chupas, C. P. Grey, *Science* **2014**, *344*, 1252817.
- [77] C. Delmas, M. Maccario, L. Croguennec, F. Le Cras, F. Weill, *Nat. Mater.* **2008**, *7*, 665.
- [78] Y. C. Lee, D.-W. Han, M. Park, M. R. Jo, S. H. Kang, J. K. Lee, Y.-M. Kang, *ACS Appl. Mater. Interfaces* **2014**, *6*, 9435.
- [79] B. Wang, W. Al Abdulla, D. Wang, X. S. Zhao, *Energy Environ. Sci.* **2015**, *8*, 869.
- [80] Y. Wang, Y. Wang, E. Hosono, K. Wang, H. Zhou, *Angew. Chem., Int. Ed.* **2008**, *47*, 7461.
- [81] C. Sun, S. Rajasekhara, J. B. Goodenough, F. Zhou, *J. Am. Chem. Soc.* **2011**, *133*, 2132.
- [82] C. Zhu, Y. Yu, L. Gu, K. Weichert, J. Maier, *Angew. Chem., Int. Ed.* **2011**, *50*, 6278.
- [83] X.-L. Wu, Y.-G. Guo, J. Su, J.-W. Xiong, Y.-L. Zhang, L.-J. Wan, *Adv. Energy Mater.* **2013**, *3*, 1155.
- [84] R. Mo, S. O. Tung, Z. Lei, G. Zhao, K. Sun, N. A. Kotov, *ACS Nano* **2015**, *9*, 5009.
- [85] W.-B. Luo, S.-L. Chou, Y.-C. Zhai, H.-K. Liu, *J. Mater. Chem. A* **2014**, *2*, 4927.
- [86] K. Zhang, Z. Hu, H. Gao, H. Feng, F. Cheng, Z. Tao, J. Chen, *Sci. Adv.* **2013**, *5*, 1676.
- [87] M. Pivko, M. Bele, E. Tchernychova, N. Z. Logar, R. Dominko, M. Gaberscek, *Chem. Mater.* **2012**, *24*, 1041.
- [88] H. Yoo, M. Jo, B.-S. Jin, H.-S. Kim, J. Cho, *Adv. Energy Mater.* **2011**, *1*, 347.
- [89] D. Choi, D. Wang, I.-T. Bae, J. Xiao, Z. Nie, W. Wang, V. V. Viswanathan, Y. J. Lee, J.-G. Zhang, G. L. Graff, Z. Yang, J. Liu, *Nano Lett.* **2010**, *10*, 2799.
- [90] S. K. Martha, J. Grinblat, O. Haik, E. Zinigrad, T. Drezon, J. H. Miners, I. Exnar, A. Kay, B. Markovsky, D. Aurbach, *Angew. Chem., Int. Ed.* **2009**, *48*, 8559.
- [91] H. Wang, Y. Yang, Y. Liang, L.-F. Cui, H. Sanchez Casalongue, Y. Li, G. Hong, Y. Cui, H. Dai, *Angew. Chem., Int. Ed.* **2011**, *50*, 7364.
- [92] Y. K. Sun, S. M. Oh, H. K. Park, B. Scrosati, *Adv. Mater.* **2011**, *23*, 5050.
- [93] S.-M. Oh, S.-T. Myung, J. B. Park, B. Scrosati, K. Amine, Y.-K. Sun, *Angew. Chem., Int. Ed.* **2012**, *51*, 1853.
- [94] R. Amisse, S. Hamelet, D. Hanzel, M. Courty, R. Dominko, C. Masquelier, *J. Electrochem. Soc.* **2013**, *160*, A1446.
- [95] N. A. Hamid, S. Wennig, A. Heinzl, C. Schulz, H. Wiggers, *Ionics* **2015**, *21*, 1857.
- [96] W. Duan, Z. Hu, K. Zhang, F. Cheng, Z. Tao, J. Chen, *Nanoscale* **2013**, *5*, 6485.
- [97] D.-W. Han, S.-J. Lim, Y.-I. Kim, S. H. Kang, Y. C. Lee, Y.-M. Kang, *Chem. Mater.* **2014**, *26*, 3644.
- [98] J. Xu, S.-L. Chou, C. Zhou, Q.-F. Gu, H.-K. Liu, S.-X. Dou, *J. Power Sources* **2014**, *246*, 124.
- [99] Y. Q. Qiao, X. L. Wang, Y. J. Mai, X. H. Xia, J. Zhang, C. D. Gu, J. P. Tu, *J. Alloys Compd.* **2012**, *536*, 132.
- [100] M. Pivko, I. Arcon, M. Bele, R. Dominko, M. Gaberscek, *J. Power Sources* **2012**, *216*, 145.
- [101] X. Zhu, Z. Yan, W. Wu, W. Zeng, Y. Du, Y. Zhong, H. Zhai, H. Ji, Y. Zhu, *Sci. Rep.* **2014**, *4*, 5768.
- [102] D. Li, M. Tian, R. Xie, Q. Li, X. Fan, L. Gou, P. Zhao, S. Ma, Y. Shi, H. T. H. Yong, *Nanoscale* **2014**, *6*, 3302.

- [103] Q. L. Wei, Q. Y. An, D. D. Chen, L. Q. Mai, S. Y. Chen, Y. L. Zhao, K. M. Hercule, L. Xu, A. Minhas-Khan, Q. J. Zhang, *Nano Lett.* **2014**, *14*, 1042.
- [104] Y. Z. Luo, X. Xu, Y. X. Zhan, Y. Q. Pi, Y. L. Zhao, X. C. Tian, Q. Y. An, Q. L. Wei, L. Q. Mai, *Adv. Energy Mater.* **2014**, *4*, 1400107.
- [105] A. Nyttén, A. Abouimrane, M. Armand, T. Gustafsson, J. O. Thomas, *Electrochem. Commun.* **2005**, *7*, 156.
- [106] H. Y. Gao, Z. Hu, K. Zhang, F. Y. Cheng, Z. L. Tao, J. Chen, *J. Energy Chem.* **2014**, *23*, 274.
- [107] H. Y. Gao, Z. Hu, J. G. Yang, J. Chen, *Energy Technol.* **2014**, *2*, 355.
- [108] H. Zhu, X. Wu, L. Zan, Y. Zhang, *ACS Appl. Mater. Interfaces* **2014**, *6*, 11724.
- [109] Z. Zheng, Y. Wang, A. Zhang, T. Zhang, F. Cheng, Z. Tao, J. Chen, *J. Power Sources* **2012**, *198*, 229.
- [110] J. Yi, M. Hou, H. Bao, C. Wang, J. Wang, Y. Xia, *Electrochim. Acta* **2014**, *133*, 564.
- [111] H. Gao, Z. Hu, K. Zhang, F. Cheng, J. Chen, *Chem. Commun.* **2013**, *49*, 3040.
- [112] M. Kuezman, S. Devaraj, P. Balaya, *J. Mater. Chem.* **2012**, *22*, 21279.
- [113] Y. Li, Z. Gong, Y. Yang, *J. Power Sources* **2007**, *174*, 528.
- [114] J. Liu, H. Xu, X. Jiang, J. Yang, Y. Qian, *J. Power Sources* **2013**, *231*, 39.
- [115] G. He, A. Manthiram, *Adv. Funct. Mater.* **2014**, *24*, 5277.
- [116] J. S. Park, K. C. Roh, J.-W. Lee, K. Song, Y.-I. Kim, Y.-M. Kang, *J. Power Sources* **2013**, *230*, 138.
- [117] Z. Hu, K. Zhang, H. Gao, W. Duan, F. Cheng, J. Liang, J. Chen, *J. Mater. Chem. A* **2013**, *1*, 12650.
- [118] M. R. Palacin, *Chem. Soc. Rev.* **2009**, *38*, 2565.
- [119] Y.-P. Wu, C.-R. Wan, C.-Y. Jiang, S.-B. Fang, Y.-Y. Jiang, *Carbon* **1999**, *37*, 1901.
- [120] Y. S. Hu, P. Adelhelm, B. M. Smarsly, S. Hore, M. Antonietti, J. Maier, *Adv. Funct. Mater.* **2007**, *17*, 1873.
- [121] J. Chen, J. Z. Wang, A. I. Minett, Y. Liu, C. Lynam, H. Liu, G. G. Wallace, *Energy Environ. Sci.* **2009**, *2*, 393.
- [122] Z.-L. Wang, D. Xu, H.-G. Wang, Z. Wu, X.-B. Zhang, *ACS Nano* **2013**, *7*, 2422.
- [123] G.-N. Zhu, H.-J. Liu, J.-H. Zhuang, C.-X. Wang, Y.-G. Wang, Y.-Y. Xia, *Energy Environ. Sci.* **2011**, *4*, 4016.
- [124] K. Song, D.-H. Seo, M. R. Jo, Y.-I. Kim, K. Kang, Y.-M. Kang, *J. Phys. Chem. Lett.* **2014**, *5*, 1368.
- [125] D. Song, M. R. Jo, G.-H. Lee, J. Song, N.-S. Choi, Y.-M. Kang, *J. Alloys Compd.* **2014**, *615*, 220.
- [126] J. M. Feckl, K. Fominykh, M. Döblinger, D. Fattakhova-Rohlfing, T. Bein, *Angew. Chem., Int. Ed.* **2012**, *51*, 7459.
- [127] X. Zhou, L.-J. Wan, Y.-G. Guo, *Adv. Mater.* **2013**, *25*, 2152.
- [128] L. Zhao, Y. Hu, H. Li, Z. Wang, L. Chen, *Adv. Mater.* **2011**, *23*, 1385.
- [129] G. Hasegawa, K. Kanamori, T. Kiyomura, H. Kurata, K. Nakanishi, T. Abe, *Adv. Energy Mater.* **2015**, *5*, 1400730.
- [130] Z. Zhu, F. Cheng, J. Chen, *J. Mater. Chem. A* **2013**, *1*, 9484.
- [131] Y. Wang, L. Gu, Y. Guo, H. Li, X. He, S. Tsukimoto, Y. Ikuhara, L. Wan, *J. Am. Chem. Soc.* **2012**, *134*, 7874.
- [132] M. R. Jo, G.-H. Lee, Y.-M. Kang, *ACS Appl. Mater. Interfaces* **2015**, *7*, 27934.
- [133] M. R. Jo, J. Jung, G.-H. Lee, Y. Kim, K. Song, J. Yang, J. S. Chae, K. C. Roh, Y.-I. Kim, W.-S. Yoon, Y.-M. Kang, *Nano Energy* **2016**, *19*, 246.
- [134] H. Ma, F. Cheng, J. Chen, J. Zhao, C. Li, Z. Tao, J. Liang, *Adv. Mater.* **2007**, *19*, 4067.
- [135] H. Wu, G. Chan, J. W. Choi, I. Ryu, Y. Yao, M. T. McDowell, S. W. Lee, A. Jackson, Y. Yang, L. Hu, Y. Cui, *Nat. Nanotechnol.* **2012**, *7*, 310.
- [136] M. Kummer, J. P. Badillo, A. Schmitz, H.-G. Brehmes, M. Winter, C. Schulz, H. Wiggers, *J. Electrochem. Soc.* **2014**, *161*, A40.
- [137] H. Ma, F. Y. Cheng, J. Chen, J. Z. Zhao, C. S. Li, Z. L. Tao, J. Liang, *Adv. Mater.* **2008**, *19*, 4067.
- [138] S. Guo, H. Li, H. Bai, Z. Tao, J. Chen, *J. Power Sources* **2014**, *248*, 1141.
- [139] L. Wei, K. Zhang, Z. Tao, J. Chen, *J. Alloys Compd.* **2015**, *644*, 742.
- [140] M. Gao, D. Wang, X. Zhang, H. Pan, Y. Liu, C. Liang, C. Shang, Z. Guo, *J. Mater. Chem. A* **2015**, *3*, 10767.
- [141] Y. Liu, R. Ma, Y. He, M. Gao, H. Pan, *Adv. Funct. Mater.* **2014**, *24*, 3944.
- [142] N. Liu, Z. Lu, J. Zhao, M. T. McDowell, H.-W. Lee, W. Zhao, Y. Cui, *Nat. Nanotechnol.* **2014**, *9*, 187.
- [143] M. Ko, S. Chae, S. Jeong, P. Oh, J. Cho, *ACS Nano* **2014**, *8*, 8591.
- [144] H. Tang, J. Zhang, Y. J. Zhang, Q. Q. Xiong, Y. Y. Tong, Y. Li, X. L. Wang, C. D. Gu, J. P. Tu, *J. Power Sources* **2015**, *286*, 431.
- [145] Y. Lee, Y.-U. Heo, D. Song, D. W. Shin, Y.-M. Kang, *Electrochim. Acta* **2014**, *118*, 100.
- [146] N. Liu, H. Wu, M. T. McDowell, Y. Yao, C. Wang, Y. Cui, *Nano Lett.* **2012**, *12*, 3315.
- [147] T. Song, H. Cheng, H. Choi, J.-H. Lee, H. Han, D. H. Lee, D. S. Yoo, M.-S. Kwon, J.-M. Choi, S. G. Doo, H. Chang, J. Xiao, Y. Huang, W. Park, Y.-C. Chung, H. Kim, J. A. Rogers, U. Paik, *ACS Nano* **2012**, *6*, 303.
- [148] L. Wang, X. M. He, J. J. Li, W. T. Sun, J. Gao, J. W. Guo, C. Y. Jiang, *Angew. Chem. Int. Ed.* **2012**, *51*, 9034.
- [149] J. Sun, G. Zheng, H. W. Lee, N. Liu, H. Wang, H. Yao, W. Yang, Y. Cui, *Nano Lett.* **2014**, *14*, 4573.
- [150] C. M. Park, H. J. Sohn, *Adv. Mater.* **2007**, *19*, 2465.
- [151] L. Wang, X. He, J. Li, W. Sun, J. Gao, J. Guo, C. Jiang, *Angew. Chem., Int. Ed.* **2012**, *51*, 9034.
- [152] Y. Lu, J.-P. Tu, Q.-Q. Xiong, J.-Y. Xiang, Y.-J. Mai, J. Zhang, Y.-Q. Qiao, X.-L. Wang, C.-D. Gu, S. X. Mao, *Adv. Funct. Mater.* **2012**, *22*, 3927.
- [153] Y. Y. Zhang, X. H. Rui, Y. X. Tang, Y. Q. Liu, J. Q. Wei, S. Chen, W. R. Leow, W. L. Li, Y. J. Liu, J. Y. Deng, B. Ma, Q. Y. Yan, X. D. Chen, *Adv. Energy Mater.* **2016**, *6*, 1502409.
- [154] M. G. Kim, S. Sim, J. Cho, *Adv. Mater.* **2010**, *22*, 5154.
- [155] Y. Xu, Q. Liu, Y. Zhu, Y. Liu, A. Langrock, M. R. Zachariah, C. Wang, *Nano Lett.* **2013**, *13*, 470.
- [156] Y. Yu, L. Gu, C. Zhu, P. A. van Aken, J. Maier, *J. Am. Chem. Soc.* **2009**, *131*, 15984.
- [157] G. Derrien, J. Hassoun, S. Panero, B. Scrosati, *Adv. Mater.* **2007**, *19*, 2336.
- [158] J. Hassoun, G. Derrien, S. Panero, B. Scrosati, *Adv. Mater.* **2008**, *20*, 3169.
- [159] N. Zhang, Q. Zhao, X. Han, J. Yang, J. Chen, *Nanoscale* **2014**, *6*, 2827.
- [160] J. Qin, C. N. He, N. Q. Zhao, Z. Y. Wang, C. S. Shi, E.-Z. Liu, J. J. Li, *ACS Nano* **2014**, *8*, 1728.
- [161] J.-W. Seo, J.-T. Jang, S.-W. Park, C. Kim, B. Park, J. Cheon, *Adv. Mater.* **2008**, *20*, 4269.
- [162] B. Huang, X. Li, Y. Pei, S. Li, X. Cao, R. C. Massé, G. Z. Cao, *Small* **2016**, *12*, 1945.
- [163] K. N. Zhao, L. Zhang, R. Xia, Y. F. Dong, W. W. Xu, C. J. Niu, L. He, M. Y. Yan, L. B. Qu, L. Q. Mai, *Small* **2016**, *12*, 588.
- [164] W. W. Xu, K. N. Zhao, C. J. Niu, L. Zhang, Z. Y. Cai, C. H. Han, L. Hen, T. Shen, M. Y. Yan, L. B. Qu, L. Q. Mai, *Nano Energy* **2014**, *8*, 196.
- [165] B. Luo, Y. Fang, B. Wang, J. S. Zhou, H. H. Song, L. J. Zhi, *Energy Environ. Sci.* **2012**, *5*, 5226.
- [166] X. Li, Z. Yang, Y. Fu, L. Qiao, D. Li, H. Yue, D. He, *ACS Nano* **2015**, *9*, 1858.
- [167] X. Wang, L. Fan, D. Gong, J. Zhu, Q. Zhang, B. Lu, *Adv. Funct. Mater.* **2016**, *26*, 1104.
- [168] D. T. Ngo, H. T. T. Le, C. Kim, J.-Y. Lee, J. G. Fisher, I.-D. Kim, C.-J. Park, *Energy Environ. Sci.* **2015**, *8*, 3577.
- [169] W. Tang, Y. Liu, C. Peng, M. Y. Hu, X. Deng, M. Lin, J. Z. Hu, K. P. Loh, *J. Am. Chem. Soc.* **2015**, *137*, 2600.

- [170] M.-S. Park, S. A. Needham, G.-X. Wang, Y.-M. Kang, J.-S. Park, S.-X. Dou, H.-K. Liu, *Chem. Mater.* **2007**, *19*, 2406.
- [171] W. W. Li, H. Q. Li, Z. J. Lu, L. Gan, L. B. Ke, T. Y. Zhai, H. S. Zhou, *Energy Environ. Sci.* **2015**, *8*, 3629.
- [172] W. Xiao, J. Zhou, L. Yu, D. H. Wang, X. W. Lou, *Angew. Chem., Int. Ed.* **2016**, *55*, 1.
- [173] P. Poizot, S. Laruelle, S. Grugeon, L. Dupont, J. M. Tarascon, *Nature* **2000**, *407*, 96.
- [174] J. Chen, L. N. Xu, W. Y. Li, X. L. Gou, *Adv. Mater.* **2005**, *17*, 582.
- [175] W. Y. Li, L. N. Xu, J. Chen, *Adv. Funct. Mater.* **2005**, *15*, 851.
- [176] Z. Hu, K. Zhang, Z. Zhu, Z. Tao, J. Chen, *J. Mater. Chem. A* **2015**, *3*, 12898.
- [177] L. X. Wang, L. Wei, Z. Tao, J. Chen, *Chin. J. Inorg. Chem.* **2014**, *30*, 2043.
- [178] Y. Liu, Y. Zhao, L. Jiao, J. Chen, *J. Mater. Chem. A* **2014**, *2*, 13109.
- [179] J. Wang, M. Gao, D. Wang, X. Li, Y. Dou, Y. Liu, H. Pan, *J. Power Sources* **2015**, *282*, 257.
- [180] Y. Xia, Z. Xiao, X. Dou, H. Huang, X. Lu, R. Yan, Y. Gan, W. Zhu, J. Tu, W. Zhang, X. Tao, *ACS Nano* **2013**, *7*, 7083.
- [181] G. Gao, L. Yu, H. B. Wu, X. W. Lou, *Small* **2014**, *10*, 1741.
- [182] C. Zhu, X. Mu, P. A. van Aken, Y. Yu, J. Maier, *Angew. Chem., Int. Ed.* **2014**, *53*, 2152.
- [183] D. Gu, W. Li, F. Wang, H. Bongard, B. Spliethoff, W. Schmidt, C. Weidenthaler, Y. Xia, D. Zhao, F. Schüth, *Angew. Chem., Int. Ed.* **2015**, *54*, 7060.
- [184] L. Xiao, M. Schroeder, S. Kluge, A. Balducci, U. Hagemann, C. Schulz, H. Wiggers, *J. Mater. Chem. A* **2015**, *3*, 11566.
- [185] L. Li, Y. Cheah, Y. Ko, P. Teh, G. Wee, C. Wong, S. Peng, M. Srinivasan, *J. Mater. Chem. A* **2013**, *1*, 10935.
- [186] L. Li, S. Peng, Y. Cheah, P. Teh, J. Wang, G. Wee, Y. Ko, C. Wong, M. Srinivasan, *Chem. Eur. J.* **2013**, *19*, 5892.
- [187] W.-B. Luo, S.-L. Chou, W. Jia-Zhao, Y.-C. Zhai, H.-K. Liu, *Sci. Rep.* **2015**, *5*, 8012.
- [188] W. X. Zhang, M. Li, Q. Wang, G. Chen, M. Kong, Z. H. Yang, S. Mann, *Adv. Funct. Mater.* **2011**, *21*, 3516.
- [189] S. Xu, C. M. Hessel, H. Ren, R. Yu, Q. Jin, M. Yang, H. Zhao, D. Wang, *Energy Environ. Sci.* **2014**, *7*, 632.
- [190] X. W. Lou, D. Deng, J. Y. Lee, J. Feng, L. A. Archer, *Adv. Mater.* **2008**, *20*, 258.
- [191] Q. Y. An, F. Lv, Q. Q. Liu, C. H. Han, K. N. Zhao, J. Z. Sheng, Q. L. Wei, M. Y. Yan, L. Q. Mai, *Nano Lett.* **2014**, *14*, 6250.
- [192] Y. M. Chen, L. Yu, X. W. Lou, *Angew. Chem., Int. Ed.* **2016**, *55*, 5990.
- [193] C. Wu, J. Maier, Y. Yu, *Adv. Mater.* **2016**, *28*, 174.
- [194] Y. Wang, L. Zhang, Y. Wu, Y. Zhong, Y. Hu, X. W. Lou, *Chem. Commun.* **2015**, *51*, 6921.
- [195] J. Wang, N. Yang, H. Tang, Z. Dong, Q. Jin, M. Yang, D. Kisailus, H. Zhao, Z. Tang, D. Wang, *Angew. Chem., Int. Ed.* **2013**, *52*, 6417.
- [196] H. Jiang, Y. Hu, S. Guo, C. Yan, P. S. Lee, C. Li, *ACS Nano* **2014**, *8*, 6038.
- [197] L. Shen, L. Yu, X.-Y. Yu, X. Zhang, X. W. Lou, *Angew. Chem., Int. Ed.* **2015**, *54*, 1868.
- [198] C. Zhu, X. Mu, P. A. van Aken, Y. Yu, J. Maier, *Angew. Chem., Int. Ed.* **2014**, *53*, 2152.
- [199] F. X. Ma, H. Hu, H. B. Wu, C. Y. Xu, Z. Xu, L. Zhen, *Adv. Mater.* **2015**, *27*, 4097.
- [200] Z. Liu, X.-Y. Yu, U. Paik, *Adv. Energy Mater.* **2016**, *6*, 1502318.